

1 **TITLE: Subthalamic-Cortical Network Reorganization during Parkinson's Tremor**

2

3 **RUNNING TITLE: Parkinson's tremor network reorganization**

4

5 **AUTHORS/AFFILIATIONS**

6 Peter M. Lauro,¹⁻³ Shane Lee,^{1,2,4} Umer Akbar,¹⁻⁵ Wael F. Asaad^{1-4,6}

7

8 ¹Department of Neuroscience, Brown University, Providence, RI 02912, USA

9 ²Robert J. and Nancy D. Carney Institute for Brain Science, Brown University, Providence, RI 02912,

10 USA

11 ³The Warren Alpert Medical School, Brown University, Providence, RI 02903, USA

12 ⁴Norman Prince Neurosciences Institute, Rhode Island Hospital, Providence, RI 02903, USA

13 ⁵Department of Neurology, Rhode Island Hospital, Providence, RI 02903, USA

14 ⁶Department of Neurosurgery, Rhode Island Hospital, Providence, RI 02903, USA

15 **Corresponding Authors:** Peter M. Lauro (peter_lauro@brown.edu), Wael F. Asaad (wfasaad@alum.mit.edu)

17

18 **Number of pages:** 37

19 **Number of figures:** 7

20 **Number of words for Abstract:** 108

21 **Number of words for Introduction:** 585

22 **Number of words for Discussion:** 1469

23

24 **Conflict of Interest:**

25 The authors have patents and patent applications broadly relevant to Parkinson's disease (but not directly
26 based upon this work). W.F.A. has received proprietary equipment and technical support for unrelated
27 research through the Medtronic external research program.

28

29 **Acknowledgements:**

30 We are grateful for the generous participation of our patients in this study. We thank Kelsea Laubenstein-
31 Parker for technical assistance, Karina Bertsch for administrative support, and Ann Duggan-Winkle for
32 clinical support. We also thank Minkyu Ahn, David Segar, Tina Sankhla, and Daniel Shiebler for help-
33 ing develop the motor task experiment. This work was supported by an NIH Training Grant (NINDS
34 T32MH020068) to P.M.L., a Doris Duke Clinical Scientist Development Award (#2014101) to W.F.A.,

35 an NIH COBRE Award: NIGMS P20 GM103645 (PI: Jerome Sanes) supporting W.F.A., a Neurosurgery
36 Research and Education Foundation (NREF) grant to W.F.A., the Lifespan Norman Prince Neurosciences
37 Institute, and the Brown University Robert J. and Nancy D. Carney Institute for Brain Science. Part of
38 this research was conducted using computational resources and services at the Center for Computation
39 and Visualization at Brown University, with funding provided by an NIH Office of the Director grant
40 S10OD025181. W.F.A. has received proprietary equipment and technical support for unrelated research
41 through the Medtronic external research program.

42 ABSTRACT

43 Tremor, a common and often primary symptom of Parkinson’s disease, has been modeled with distinct
44 onset and maintenance dynamics. To identify the neurophysiologic correlates of each state, we acquired
45 intraoperative cortical and subthalamic nucleus recordings from ten patients performing a naturalistic
46 visual-motor task. From this task we isolated short epochs of tremor onset and sustained tremor. Com-
47 paring these epochs, we found that the subthalamic nucleus was central to tremor onset, as it drove both
48 motor cortical activity and tremor output. Once tremor became sustained, control of tremor shifted to
49 cortex. At the same time, changes in directed functional connectivity across sensorimotor cortex further
50 distinguished the sustained tremor state.

51

52 SIGNIFICANCE STATEMENT

53 Tremor is a common symptom of Parkinson’s disease (PD). While tremor pathophysiology is thought to
54 involve both basal ganglia and cerebello-thalamic-cortical circuits, it is unknown how these structures
55 functionally interact to produce tremor. In this manuscript, we analyzed intracranial recordings from
56 the subthalamic nucleus and sensorimotor cortex in patients with PD undergoing deep brain stimulation
57 (DBS) surgery. Using an intraoperative task, we examined tremor in two separate dynamic contexts:
58 when tremor first emerged, and when tremor was sustained. We believe that these findings reconcile sev-
59 eral models of Parkinson’s tremor, while describing the short-timescale dynamics of subcortical-cortical
60 interactions during tremor for the first time. These findings may describe a framework for developing
61 proactive and responsive neurostimulation models for specifically treating tremor.

62

63 INTRODUCTION

64 Tremor, a cardinal symptom of Parkinson’s disease (PD), typically manifests as a 4–6 Hz oscillatory move-
65 ment of the distal limbs during rest or sustained posture (Lance et al., 1963). While often the presenting
66 motor symptom of PD, tremor (and its response to dopamine replacement therapy) is highly variable
67 across patients (Koller, 1984; Zach et al., 2015; Koller, 1986; Dirx et al., 2017; Dirx et al., 2019). PD
68 tremor neurophysiology has been described by the “dimmer switch” model where an “on-off” mechanism
69 is separable from a magnitude controller (Helmich et al., 2012). Specifically, functional MRI (fMRI)
70 BOLD activity from basal ganglia nuclei such as the globus pallidus *pars interna* (GPi) correlates with
71 the presence or absence of tremor, whereas immediate tremor amplitude better correlates with BOLD
72 signal from structures in cerebello-thalamo-cortical circuits such as motor cortex (Helmich et al., 2011;
73 Helmich, 2018). The GPi, and the monosynaptically-connected subthalamic nucleus (STN) (Albin et al.,
74 1989), are common therapeutic targets for deep brain stimulation (DBS). Indeed, DBS in each nucleus
75 is equally effective in reducing tremor (Wong et al., 2020). However, the precise role of the STN and its

76 interactions with cortex in these tremor dynamics is unknown.

77 Low-frequency (4–8 Hz) oscillatory bursting has been observed in both in the STN and GPi in MPTP
78 primate models of PD (Bergman et al., 1994; Raz et al., 2000). This bursting, although present in the
79 absence of tremor, becomes highly synchronized with tremor once it emerges. STN recordings from
80 patients with PD have similarly revealed θ /tremor-frequency (3–8 Hz) activity that is coherent with
81 electromyography (EMG) recordings of tremulous limbs (Levy et al., 2000; Reck et al., 2009; Reck et
82 al., 2010). Accordingly, STN tremor frequency oscillations (along with higher frequency oscillations)
83 have been used to predict clinical measures of tremor (Hirschmann et al., 2016; Telkes et al., 2018;
84 Asch et al., 2020). Further, studies applying STN DBS at tremor frequencies entrained tremor to the
85 phase of the stimulation, consistent with a direct modulatory role of STN on tremor (Cagnan et al.,
86 2014).

87 At the same time, tremor reorganizes cortical activity. Magnetoencephalography (MEG) studies of
88 patients with PD identified a broad cortical tremor network comprising “intrinsic” (ventrolateral anterior
89 thalamus (VLa), premotor and motor cortex) and “extrinsic” (cerebellum, ventrolateral intermedius
90 (VIM), somatosensory cortex) loops hypothesized to initialize and stabilize tremor respectively (Volkman
91 et al., 1996; Timmermann et al., 2003). This cortico-cortical synchronization at single and double tremor
92 frequencies extends to STN local field potential (LFP) and EMG recordings as well (Hirschmann et
93 al., 2013). Meanwhile, intraoperative studies combining electrocorticography (ECoG) and STN LFP
94 recordings found decreases in α (8–13 Hz) and β (13–30 Hz) coherence during tremor (Qasim et al., 2016).
95 Despite this broad cortico-cortical synchronization at tremor frequencies, it remains unclear whether these
96 neurophysiological changes are specific to tremor onset or maintenance. In addition, although STN and
97 sensorimotor cortex become coherent during tremor, the manner in which tremor-related activity is
98 coordinated across structures, and how different networks of activity may reflect the different stages of
99 tremor production and maintenance, are unknown.

100 Thus, in order to understand whether there are indeed distinct neurophysiological mechanisms of
101 tremor initiation and maintenance, and to better understand what neurophysiological interactions char-
102 acterize these states, we recorded local field potential activity from the STN along with ECoG from
103 sensorimotor cortices while subjects with PD engaged in a task that elicited initiation and persistence
104 of tremor. Specifically, we tested whether the STN (like the GPi) drove tremor specifically during onset,
105 while cortical structures drove sustained tremor.

106

107 **MATERIALS AND METHODS**

108 **Participants**

109 All patients undergoing routine, awake placement of deep brain stimulating electrodes for intractable,

110 idiopathic PD between November 2015 and September 2017 were invited to participate in this study
111 (**Table 1**). Patients with PD were selected and offered the surgery by a multi-disciplinary team based
112 solely upon clinical criteria, and the choice of the target (STN vs. GPi) was made according to each
113 patient's particular circumstance (disease manifestations, cognitive status and goals) (Akbar and Asaad,
114 2017). In this report, we focused on ten patients (9M, 1F) undergoing STN DBS with intraoperative
115 ECoG recordings. Patients were off all anti-Parkinsonian medications for at least 12 hours in advance of
116 the surgical procedure (UPDRS Part III: 48.2 ± 15.6). Four patients were considered tremor-dominant,
117 and six patients had average tremor UPDRS III scores > 2 in their right hand (Jankovic et al., 1990).
118 Approximately age-matched controls (3M, 11F; often patients' partners) also participated in this study
119 ($n = 14$ subjects); patients were aged 55.6–78.5 years (65.2 ± 7.4), and controls were aged 48.3–79.2 years
120 (62.4 ± 10.0) at the time of testing (Mann-Whitney U-test, $p > 0.05$). Controls were required simply to
121 be free of any diagnosed or suspected movement disorder and to have no physical limitation preventing
122 them from seeing the display or manipulating the joystick. There was a strong male-bias in the patient
123 population (9M, 1F) and a female preponderance in the control population (3M, 11F), reflecting weaker
124 overall biases in the prevalence of PD and the clinical utilization of DBS therapy (Accolla et al., 2007;
125 Hariz et al., 2011; Rumalla et al., 2018). All subjects were right-handed. Patients and other subjects
126 agreeing to participate in this study signed informed consent, and experimental procedures were under-
127 taken in accordance with an approved Rhode Island Hospital human research protocol (Lifespan IRB
128 protocol #263157) and the Declaration of Helsinki.

129

130 **Surgical Procedure**

131 Microelectrode recordings (MER) from the region of the STN of awake patients are routinely obtained in
132 order to map the target area and guide DBS electrode implantation. A single dose of short-acting seda-
133 tive medication (typically propofol) was administered before the start of each procedure, at least 60–90
134 minutes prior to MER. The initial trajectory was determined on high-resolution (typically 3T) magnetic
135 resonance images (MRI) co-registered with CT images demonstrating previously-implanted skull-anchor
136 fiducial markers (version 3.0, FHC Inc., Bowdoin, ME, USA). Localization of the target relied upon a
137 combination of direct and indirect targeting, utilizing the visualized STN as well as standard stereotactic
138 coordinates relative to the anterior and posterior commissures. Appropriate trajectories to the target
139 were then selected to avoid critical structures and to maximize the length of intersection with the STN.
140 A 3-D printed stereotactic platform (STarFix micro-targeting system, FHC Inc.) was then created such
141 that it could be affixed to these anchors, providing a precise trajectory to each target (Konrad et al.,
142 2011). Microdrives were attached to the platform and then loaded with microelectrodes. Recordings were
143 typically conducted along the anterior, center, and posterior trajectories (with respect to the initial MRI-

144 determined trajectory) separated by 2 mm, corresponding to the axis of highest anatomical uncertainty
145 based upon the limited visualization of the STN on MRI. Bilateral electrocorticography (ECoG) strips
146 were placed posteriorly along sensorimotor cortices through the same burr hole used for MER insertion
147 for temporary recordings. MER began about 10–12 mm above the MRI-estimated target, which was
148 chosen to lie near the inferior margin of the STN, about 2/3 of the distance laterally from its medial
149 border. The STN was identified electrophysiologically as a hyperactive region typically first encountered
150 about 3–6 mm above estimated target (Gross et al., 2006). At variable intervals, when at least one elec-
151 trode was judged to be within the STN, electrode movement was paused in order to assess neural activity
152 and determine somatotopic correspondence, as per routine clinical practice. At these times, if patients
153 were willing and able, additional recordings were obtained in conjunction with patient performance of
154 the visual-motor task.

155

156 **Neurophysiological Signals and Analysis**

157 Microelectrode signals were recorded using “NeuroProbe” tungsten electrodes (Alpha Omega, Nazareth,
158 Israel). ECoG signals were acquired using Ad-Tech 8-contact subdural strips with 10 mm contact-to-
159 contact spacing (Ad-Tech Medical, Racine, WI). All signals were acquired at 22–44 kHz and synchronized
160 using Neuro Omega data acquisition systems (Alpha Omega). Microelectrode impedances were typically
161 400–700 k Ω while ECoG contact impedances were typically 10–30 k Ω . Patients performed up to 4 sessions
162 of the task, with microelectrodes positioned at different depths for each session. As microelectrodes were
163 not independently positionable, some signals may have necessarily been acquired outside of the STN. All
164 recorded signals were nevertheless considered and analyzed.

165 Neural data were analyzed using the “numpy/scipy” Python 3 environment (Harris et al., 2020;
166 Virtanen et al., 2020) (<https://numpy.org/>, <https://www.scipy.org/>). Offline, ECoG contacts were
167 re-referenced to a common median reference within a strip (Liu et al., 2015). All resulting signals were
168 bandpass filtered between 2–600 Hz, and notch filtered at 60 Hz and its harmonics. Timeseries were
169 Z-scored and artifacts above 4 standard deviations were removed. These resulting timeseries were then
170 downsampled to 1 kHz. Timeseries were bandpass filtered using a Morlet wavelet convolution (wave
171 number 7) at 1 Hz intervals, covering 3–400 Hz. The instantaneous power and phase at each frequency
172 was then acquired by the Hilbert transform. To analyze broad frequency bands, we grouped frequencies
173 as: θ : 3–8 Hz, α : 8–12 Hz, β_{low} : 12–20 Hz, β_{high} : 20–30 Hz, γ_{low} : 30–60 Hz, γ_{mid} : 60–100 Hz, γ_{high} :
174 100–200 Hz, and hfo : 200–400 Hz. For interregional analyses (phase-locking value, phase slope index, and
175 granger prediction) we focused on frequencies up to 100 Hz; spectral or timeseries data were subsequently
176 downsampled to 250 Hz.

177

178 **Anatomical Reconstruction of Recording Sites**

179 Patients underwent pre-, intra- and post-operative imaging per routine clinical care. Preoperatively,
180 stereotactic protocol magnetic resonance (MR) images were obtained (Siemens Vario 3.0 T scanner) that
181 included T1- and T2-weighted sequences (T1: MPRAGE sequence; TR: 2530 ms, TE: 2.85 ms, matrix
182 size: 512 x 512, voxels: 0.5 x 0.5 mm² in-plane resolution, 224 sagittal slices, 1 mm slice thickness;
183 T2: SPACE sequence, TR: 3200 ms, TE: 409 ms, matrix size: 512 x 512, voxels: 0.5 x 0.5 mm² in-plane
184 resolution, 224 sagittal slices, 1 mm slice thickness). Pre-, intra-, and post-operative (in some cases) com-
185 puted tomography (CT) scans were also acquired (Extra-Op CT: GE Lightspeed VCT Scanner; Tube
186 voltage: 120 kV, Tube current: 186 mA, data acquisition diameter: 320 mm, reconstruction diameter:
187 250 mm, matrix size: 512 x 512 voxels, 0.488 x 0.488 mm² in-plane resolution, 267 axial slices, 0.625
188 mm slice thickness; Intra-Op CT: Mobius Airo scanner, Tube voltage: 120 kV, Tube current: 240 mA,
189 data acquisition diameter: 1331 mm, reconstruction diameter: 337 mm, matrix size: 512 x 512 voxels,
190 0.658 x 0.658 mm² in-plane resolution, 182 axial slices, 1 mm slice thickness). Postoperative MR images
191 (Seimens Aera 1.5 T scanner, T1: MPRAGE sequence, TR: 2300 ms, TE: 4.3 ms, matrix size: 256 x
192 256 voxels, 1.0 x 1.0 mm² in-plane resolution, 183 axial slices, 1 mm slice thickness, specific absorption
193 rate < 0.1 W/g) were typically obtained 1–2 days after the operation to confirm proper final electrode
194 location.

195 To reconstruct recording locations, MR and CT images were co-registered using the FHC Waypoint
196 Planner software. The raw DICOM images and the linear transform matrices were exported and applied
197 to reconstructed image volumes using the AFNI command “3dAllineate,” bringing them into a common
198 coordinate space (Cox, 1996; Li et al., 2016). Microelectrode depths were calculated by combining
199 intraoperative recording depth information with electrode reconstructions obtained from postoperative
200 images using methods described previously (Lauro et al., 2015; Lauro et al., 2018). To determine the
201 anatomical distribution of microelectrode recording sites across patients, preoperative T1-weighted MR
202 images were registered to a T1-weighted MNI reference volume (MNI152_T1_2009c) using the AFNI
203 command “3dQwarp” (Fonov et al., 2009). The resulting patient-specific transformation was then applied
204 to recording site coordinates. MNI-warped recording coordinates were then assessed for proximity to
205 structures such as the STN as delineated on the MNI PD25 atlas (Xiao et al., 2012; Xiao et al., 2015;
206 Xiao et al., 2017). ECoG contacts were segmented from intraoperative CT volumes using the same
207 DBStar processing as microelectrodes. Contacts were then projected onto individual cortical surface
208 reconstructions generated from preoperative T1 volumes (Dale et al., 1999; Fischl et al., 2002; Saad and
209 Reynolds, 2012; Trotta et al., 2018). Individual cortical surface reconstructions were co-registered to a
210 standard Desikan-Destrieux surface parcellation (Argall et al., 2006; Desikan et al., 2006; Destrieux et
211 al., 2010). Contacts were labeled and grouped as “premotor cortex,” “motor cortex,” “somatosensory

212 cortex,” or “parietal cortex” if they contained the following anatomical parcellation labels:

- 213 • Premotor cortex/PMC : ctx_lh_G_front_sup, ctx_lh_G_front_middle
- 214 • Motor cortex/MC : ctx_lh_G_precentral
- 215 • Somatosensory cortex/SC : ctx_lh_G_postcentral
- 216 • Posterior Parietal cortex/PPC : ctx_lh_G_parietal_sup, ctx_lh_G_pariet_inf-Supramar

217 If a contact had more than one label (8/80 contacts), they were removed from further analysis.

218

219 **Experimental Design**

220 We employed a visual-motor target tracking task to estimate the degree of motor dysfunction in a continu-
221 ous fashion. Specifically, while patients with PD reclined on the operating bed in a “lawn-chair” position,
222 a joystick was positioned within their dominant hand, and a boom-mounted display was positioned within
223 their direct line-of-sight at a distance of ~1 meter. The task was implemented in MonkeyLogic (Asaad
224 and Eskandar, 2008a; Asaad and Eskandar, 2008b; Asaad et al., 2013) and required subjects to follow a
225 green target circle that moved smoothly around the screen by manipulating the joystick with the goal of
226 keeping the white cursor within the circle (**Figure 1A**). The target circle followed one of several possible
227 paths (invisible to the subject), with each trial lasting 10–30 seconds. Each session consisted of up to 36
228 trials (~13 minutes of tracking data), and subjects performed 1–4 sessions during the operation. Control
229 subjects performed this task in an extra-operative setting.

230

231 **Speed Quantification**

232 To calculate movement speed, x- and y-joystick traces were 3 Hz low-pass filtered, and the euclidean
233 change of cursor position was calculated over time. To standardize movement speed within patients,
234 movement speed values within a session were min-max normalized into a measure of “slowness,” where
235 0=highest speed and 1=lowest speed.

236

237 **Tremor Amplitude Quantification**

238 To calculate tremor, x- and y-joystick traces were 3–8 Hz bandpass filtered, and a one-dimensional linear
239 projection of the filtered traces was calculated. Tremor amplitude and phase were calculated using the
240 Hilbert transform of the resulting one-dimensional timeseries.

241

242 **Tremor Epoch Design**

243 To standardize tremor amplitude across patients, tremor amplitude values from controls and patients
244 were averaged into 4 second contiguous, non-overlapping epochs. The resulting average and standard

245 deviation of the control tremor amplitude distribution were used to Z-transform control subject and PD
246 patient tremor amplitude epochs (**Figure 1B**). To determine a cutoff to optimally differentiate control
247 and PD population tremor data, receiver operator characteristic (ROC) tests were performed between
248 supra-cutoff population data for cutoff values ranging from -2 (the lowest observed in both populations)
249 and 10. The maximum area-under-curve (AUC) value was observed for $Z=3$ (ROC AUC = 0.85), which
250 was used for subsequent analyses.

251

252 To analyze neural activity associated with different tremor dynamics, 4 second tremor epochs were defined
253 as following:

- 254 • “No Tremor” epochs were characterized by tremor staying below a 3 s.d. threshold for 4 seconds.
- 255 • “Tremor Onset” epochs were characterized by tremor exceeding a 3 s.d. threshold for 2 seconds,
256 with tremor in the preceding 2 seconds being sub-threshold.
- 257 • “Sustained Tremor” epochs were characterized by tremor staying above a 3 s.d. threshold for 4
258 seconds.

259 All epochs were non-overlapping in time.

260

261 **Tremor Frequency Calculation and UPDRS Correlation**

262 To calculate each patient’s dominant tremor frequency (i.e. the frequency with the largest amplitude), a
263 distribution of tremor amplitude was created by aggregating each patient’s tremor amplitude epochs. In
264 parallel, a frequency distribution was created by calculating the dominant tremor frequency within each
265 epoch. A patient-specific dominant tremor frequency was then calculated as the frequency containing the
266 highest aggregate tremor amplitude.

267 Correlations between task-derived tremor and UPDRS were conducted with sub-scores pertaining to
268 the upper extremity relevant to the patient’s task performance (Rest Tremor, Postural Tremor, Finger
269 Taps, Hand Opening/Closing, Rapid Alternating Movements (RAM), Rigidity). Each patient UPDRS
270 sub-score was Spearman correlated with the median of each patient’s tremor amplitude distribution, and
271 was assessed for significance using a bootstrap null distribution where tremor medians were randomly
272 shuffled with respect to UPDRS sub-scores.

273

274 **Tremor/Speed-Spectral Power Correlation**

275 To determine if spectral power across frequencies correlated with changes in tremor amplitude or slow-
276 ness, Spearman correlations were calculated between 4 second epochs of averaged tremor/slowness and
277 spectral magnitude of narrowbands with 1 Hz bandwidth. Correlations were calculated within entire task

278 sessions. To determine whether spectral-tremor correlations were consistently positive or negative across
279 all sessions, ρ -value distributions were tested for asymmetry about zero using Wilcoxon tests (Wilcoxon
280 p-values corrected by the Benjamini-Hochberg procedure at $q = 0.05$).

281

282 Tremor Epoch Spectral Power Modulation

283 To determine if spectral power at each structure differed by tremor epoch type, spectral power across
284 frequencies were compared using the Kruskal-Wallis test. If spectral power in a frequency band was
285 found to significantly differ across epoch types, pairwise post-hoc Conover tests between tremor epochs
286 were performed using the “scikit-posthocs” python toolbox. (Terpilowski, 2019) ([https://github.com/](https://github.com/maximtrp/scikit-posthocs)
287 [maximtrp/scikit-posthocs](https://github.com/maximtrp/scikit-posthocs)). P-values < 0.05 from post-hoc tests were considered significant.

288

289 Tremor-Neural θ Phase Locking Value

290 To determine whether θ (3–8 Hz) in tremor and neural recordings were synchronized, the phase-locking
291 value (PLV) was calculated with tremor and neural θ phase per trial (Lachaux et al., 1999). θ phase
292 estimates for neural spectral data were calculated by taking the circular/angular mean for narrowband
293 phase estimates between 3–8 Hz at each timepoint (t).

$$PLV_{Tremor-Neural\theta} = \frac{1}{T} \left| \sum_{t=1}^T e^{i(\theta_{Tremor}(t) - \theta_{Neural}(t))} \right| \quad (1)$$

294 All PLV-related analyses were also calculated with the pairwise phase consistency (PPC) measure to
295 control for differences in number of trials across conditions (Vinck et al., 2010; Aydore et al., 2013).

$$PPC = \frac{N_{trials}}{N_{trials} - 1} \left(PLV^2 - \frac{1}{N_{trials}} \right) \quad (2)$$

296 As PLV and PPC results were qualitatively similar, we reported PLV results.

297

298 Tremor-Neural θ Phase Slope Index

299 To understand the lag-lead relationship between tremor (a bandpassed signal) and neural θ phase locking,
300 the phase slope index (PSI) was calculated for the θ band (3–8 Hz) with 1 Hz frequency resolution (Nolte
301 et al., 2008) using the “spectral_connectivity” python toolbox ([https://github.com/Eden-Kramer-Lab/](https://github.com/Eden-Kramer-Lab/spectral_connectivity)
302 [spectral_connectivity](https://github.com/Eden-Kramer-Lab/spectral_connectivity), <https://doi.org/10.5281/zenodo.4088934>).

303 As the “spectral_connectivity” toolbox uses the multitaper transform for spectral analysis, the number
304 of necessary tapers (L) was calculated by first calculating the time-half-bandwidth product (TW) using
305 the desired frequency resolution (Δf , 1 Hz for parity with wavelet spectral analyses) and the time window

306 of the entire trial (N , 4 seconds) (Prerau et al., 2016).

$$TW = \frac{N\Delta f}{2} \quad (3)$$

307 We subsequently used TW to calculate the number of tapers (L) using the floor function.

$$L = \lfloor 2TW - 1 \rfloor \quad (4)$$

308 With our parameters, 3 Slepian tapers were used for whole-trial single-window PSI estimates.

$$PSI_{Tremor,Neural} = \Im \left(\sum_{f \in F} C_{Tremor,Neural}^*(f) \cdot C_{Tremor,Neural}(f + \Delta f) \right) \quad (5)$$

309 PSI was then estimated from the imaginary (\Im) component of the complex coherency (C) between
 310 tremor and neural θ , where the complex coherency was calculated from the cross-spectral density matrix
 311 (S) between the two signals.

$$C_{Tremor,Neural}(f) = \frac{S_{Tremor,Neural}(f)}{\sqrt{S_{Tremor,Tremor}(f) \cdot S_{Neural,Neural}(f)}} \quad (6)$$

312 Phase offsets between 1 Hz frequency bands (Δf) within θ (F) were used to calculate the phase slope.
 313 Because of our short-timescale windowed application of PSI, we did not normalize values of PSI by their
 314 standard deviation (Young et al., 2017). To determine if tremor or neural recordings exhibited direc-
 315 tional θ influence, the empirical PSI was compared to a null distribution of 1000 PSI values generated
 316 from shuffling one signal's timeseries across trials. P-values were calculated empirically from the result-
 317 ing distribution and corrected for multiple comparisons with the Benjamini-Hochberg method at $q = 0.05$.

318

319 Tremor Epoch Interregional Phase Locking Value

320 To compare time-varying phase synchrony across structures, the phase-locking value (PLV) was calcu-
 321 lated across each structure pair (j, k) per 1 Hz frequency band (f) from 1–100 Hz using wavelet-derived
 322 spectral data.

$$PLV_f(t) = \frac{1}{N_{trials}} \left| \sum_{n=1}^{N_{trials}} e^{i(\theta_j(f,t,n) - \theta_k(f,t,n))} \right| \quad (7)$$

323 To determine if pairwise PLV differed by tremor epoch type, PLV values within frequencies were averaged
 324 across time, and were then compared using the Kruskal-Wallis test. If PLV in a frequency band was found
 325 to significantly differ across tremor epochs, pairwise post-hoc Conover tests between tremor epochs were
 326 performed ($p < 0.05$ in post-hoc tests were deemed significant).

327

328 Tremor Epoch Interregional Granger Prediction

329 To understand whether tremor epoch-related dynamic changes in spectral power or synchrony were driven
330 by dynamic directional influences of one structure onto another, nonparametric spectral granger predic-
331 tion (GP) was calculated between each structure pair using the “spectral_connectivity” python toolbox.
332 Specifically, frequency information (1 Hz frequency resolution) for each structure-timeseries pair were cal-
333 culated using a single 4000 ms multitaper window (3 tapers). From there, a frequency-based estimation
334 of information flow between structures was calculated using a cross-density spectral matrix (Dhamala
335 et al., 2008). Subsequently, frequency-specific (f) GP (i.e. the log-ratio of total frequency power over
336 non-predicted frequency power) was calculated between structure pairs (j, k) for each epoch type using
337 the cross-spectral density matrix (S), the spectral transfer matrix (H), and the noise covariance matrix
338 (Σ).

$$GP_{j \rightarrow k}(f) = \ln \left(\frac{S_{kk}(f)}{S_{kk}(f) - (\sum_{jj} - \frac{\sum_{jk}^2}{\sum_{kk}}) |H_{jk}(f)|^2} \right) \quad (8)$$

339 To determine if one structure exhibited frequency-specific granger prediction on another, the empirical
340 GP was compared to a null distribution of 1000 GP values generated from shuffling one structure’s time-
341 series across trials. P-values for each frequency were calculated empirically from the resulting distribution
342 and corrected for multiple comparisons with the Benjamini-Hochberg method at $q = 0.05$.

343 To understand how GP varied as a function of time, frequency information for each structure-timeseries
344 pair were calculated in 2000 ms windows with 100 ms overlap using the multitaper transform for each
345 event trial. To maintain the same number of tapers (3 tapers) between static and dynamic GP analyses,
346 frequency resolution was increased to 2 Hz for dynamic GP calculation. To determine if one structure
347 exhibited time-varying directional influence on another, the empirical GP was compared to a null distri-
348 bution of 1000 GP values generated from shuffling one structure’s timeseries across trials. P-values for
349 each time and frequency point were calculated empirically from the resulting distribution and corrected
350 for multiple comparisons with the Benjamini-Hochberg method at $q = 0.05$. Resulting significant time-
351 frequency clusters were additionally filtered by only considering clusters whose area was greater than the
352 95th percentile of all BH-corrected significant clusters.

353

354 Tremor Epoch Interregional Phase Slope Index

355 In order to calculate θ directed connectivity across structures, the phase slope index (PSI) was used for
356 the θ band (3–8 Hz) with 1 Hz frequency resolution across structures. Frequency information (1 Hz fre-
357 quency resolution) for each structure-timeseries pair were calculated in a single 4000 ms window using the
358 multitaper transform (3 tapers) for each event trial. To determine if one structure exhibited PSI influence
359 on another, the empirical PSI was compared to a null distribution of 1000 PSI values generated from

360 shuffling one structure's timeseries across trials. P-values were calculated empirically from the resulting
361 distribution and corrected for multiple comparisons with the Benjamini-Hochberg method at $q = 0.05$.

362 In order to calculate time-varying PSI between broad frequency bands, PSI was calculated using a
363 2000 ms window sliding by 100 ms (3 tapers with 2 Hz frequency resolution). A bootstrap was then
364 performed, and empirical p-values for each time point were corrected for multiple comparisons with the
365 Benjamini-Hochberg method at $q = 0.05$.

366

367 **Statistical Analysis**

368 Data in text are represented as mean \pm standard deviation. All statistical tests, unless otherwise specified,
369 were carried out in the "scipy" python environment. P-values were controlled for multiple comparisons
370 by using the Benjamini-Hochberg procedure at $q = 0.05$ (Benjamini and Hochberg, 1995).

371

372 **Data and Code Accessibility**

373 The datasets supporting the current study have not been deposited in a public repository because they
374 contain patient information but are available along with analysis code upon request.

375

376 **RESULTS**

377 **Intraoperative behavioral and neural data acquisition**

378 Ten patients with PD undergoing DBS implantation and 14 age-matched control subjects (see *Methods*)
379 performed a simple visual-motor task where they followed an onscreen target using a joystick-controlled
380 cursor with their dominant hand (**Figure 1A**). Each patient performed 1–4 sessions of this target-
381 tracking task during the procedure for a total of 27 sessions, while control subjects performed 1 session
382 each for a total of 14 sessions. Tremor amplitude and cursor speed were quantified continuously from
383 the x- and y-joystick traces. The resulting PD and control tremor and speed distributions were distinct
384 (tremor: $p = 2.15 \times 10^{-154}$, speed: $p = 3.44 \times 10^{-61}$, Mann-Whitney U-test) (**Figure 1B-C**). The partial
385 overlap of the PD and control tremor distributions (indicative of periods without tremor in PD patients),
386 along with the long right tail of the PD distribution, gave us a large dynamic range of tremor to analyze
387 with respect to neural data. The dominant tremor frequency across patients was 4.48 ± 0.57 Hz. While
388 tremor amplitude correlated with the resting tremor UPDRS sub-score (Spearman $\rho = 0.92, p < 0.001$,
389 bootstrap test), it did not with the postural tremor sub-score ($\rho = 0.54, p = 0.065$, bootstrap test). Based
390 on the distinct tremor frequency peak and its correlation with clinical measures of resting tremor, we
391 interpreted our task-derived tremor as reflective of resting tremor (Dirkx et al., 2018).

392 Across the 10 patients with PD, we obtained 81 microelectrode recordings within the STN (peak
393 recording density: MNI $x = +13, y = +11, z = -5$; **Figure 1D**) as well as 72 ECoG recordings from

394 cortex, including premotor cortex (PMC, $n = 27$ recordings), motor cortex (MC, $n = 16$), somatosensory
395 cortex (SC, $n = 15$), and posterior parietal cortex (PPC, $n = 14$) (**Figure 1E**). All recordings were
396 contralateral to the hand used to perform the task.

397

398 **Tremor is a neurophysiologically distinct motor feature of Parkinson's disease**

399 To understand the relationship of broadband neural activity to tremor expression, we examined the
400 correlation between tremor amplitude and spectral power in neurophysiological recordings. Sorting
401 session-wide spectral data by tremor epochs (rather than according to time) revealed informative band-
402 specific patterns of activity (**Figure 2A**). Specifically, across cortical structures, spectral power in narrow
403 (1 Hz bandwidth) bands within the β range was found to negatively correlate with tremor amplitude
404 ($p \leq 0.008$, Spearman ρ) (**Figure 2B**). Interestingly, β power appeared to drop off fairly quickly with
405 even low levels of tremor becoming evident (SC - power curve fit : $r^2 = 0.77$, linear fit : $r^2 = 0.54$). Mean-
406 while, θ power positively correlated with tremor amplitude in PMC ($p = 0.005$) and SC ($p \leq 0.005$).
407 Power in all bands except β_{high} positively correlated with tremor in STN recordings ($p \leq 0.012$).

408 To compare tremor-related neural activity with a distinct PD motor feature (specifically bradykine-
409 sia), neural data were also analyzed with respect to movement “slowness” during the same target-tracking
410 task. Note that PD subjects appeared to lack a higher mode of movement velocity that was clearly present
411 in control subjects, reflecting an inability to move the cursor consistently as quickly as the target (**Figure**
412 **1C**). We calculated a min-max normalized measure of inverse cursor speed (0=highest speed, 1=lowest
413 speed) to capture this effect as a positive pathological sign, parallel to the sign of tremor. In contrast
414 to tremor, we observed positive correlations between slowness and α/β (8–30 Hz) power in all cortical
415 structures ($p \leq 0.001$) (**Figure 2B**). However, θ did not show a significant correlation with slowness
416 in any structure ($p > 0.05$). Thus, θ appeared to relate specifically to tremor, whereas the relationship
417 to β activity was generally reversed between these PD-related motor manifestations. So while there was
418 broadly the appearance of a symmetric opposition between tremor and slowness in terms of their correla-
419 tions with neural activity across frequencies (**Figure 2B**), this difference in the θ frequency relationship,
420 as well as perhaps a consistent difference in γ_{mid} (in which the correlation with tremor was typically
421 close to 0 but the correlation with slowness was typically greater in magnitude and negative in direction),
422 suggest these motor features are not simply opposite ends of a single spectrum but rather have distinct
423 fingerprints in neural activity.

424

425 **Subthalamic θ preceded tremor at onset**

426 Because lower frequency oscillations, particularly θ , were most consistently and strongly positively as-
427 sociated with tremor across structures, and because they encompassed the range of observed tremor

428 frequencies from a behavioral perspective (4–6 Hz), we next turned our attention to understanding the
429 relationship of θ band activity within each structure to tremor-defined epochs. Using a control vs. PD
430 subject ROC-derived tremor threshold (see *Methods*), behavioral and spectral data were organized into
431 4 second epochs and categorized as: no tremor epochs (575 epochs, 2300 sec), tremor onset epochs (406
432 epochs, 1624 sec), and sustained tremor epochs (171 epochs, 684 sec) (**Figure 3A**). STN θ power was
433 indeed significantly elevated during tremor onset and sustained tremor, relative to no tremor (1.07–2.49
434 fold increase, $p \leq 0.011$, Kruskal-Wallis test, $p < 0.05$, Conover test for post-hoc comparisons) (**Figure**
435 **3B**). Likewise, phase synchrony (measured as phase locking value, or PLV) between STN θ and tremor
436 was increased during tremor onset and sustained tremor ($p = 7.20 \times 10^{-39}$, Kruskal-Wallis test, $p < 0.05$,
437 Conover test) (**Figure 4A**).

438 In light of this close relationship between STN θ and tremor, we next examined the temporal re-
439 lationship between STN θ and tremor phase. Specifically, we calculated the phase-slope index (PSI)
440 between tremor and STN θ phase. Because the PSI considers multiple phase relationships within a range
441 of frequencies, it can succeed in determining the net leading or lagging oscillation in a manner that avoids
442 the circularity problem inherent in methods such as the PLV (Nolte et al., 2008). Here, the PSI revealed
443 STN θ led tremor exclusively during tremor onset ($p = 0.011$, bootstrap test) (**Figure 4B**), consistent
444 with a causal role for the STN in the initiation but not necessarily the maintenance of tremor.

445 **Somatosensory cortex θ consistently followed tremor**

446 Like the STN, SC θ power positively correlated with tremor amplitude. Therefore we investigated if this
447 spectral-tremor relationship varied similarly with tremor state. SC θ power was indeed significantly ele-
448 vated during tremor onset and sustained tremor, relative to no tremor (1.08–1.93 fold increase, $p \leq 2.35$
449 $\times 10^{-9}$, Kruskal-Wallis test, $p < 0.05$, Conover test) (**Figure 3B**). SC-tremor θ PLV also was increased
450 during tremor onset and sustained tremor ($p = 4.03 \times 10^{-37}$, Kruskal-Wallis test, $p < 0.05$, Conover test)
451 (**Figure 4A**).

452 However, in contrast to the STN, phase-slope analysis of tremor and SC θ phase revealed that SC
453 θ phase followed tremor phase during both tremor onset and sustained tremor ($p \leq 0.002$, bootstrap
454 test) (**Figure 4B**). Therefore, the strong tremor-related θ oscillation seen in SC was reflective rather
455 than causal of tremor.

456 **Motor cortex θ consistently preceded tremor**

457
458 Unlike the STN and SC, MC θ power did not show a clear graded relationship with tremor magni-
459 tude (**Figure 2**). Nonetheless, examining MC θ power across tremor states did reveal it was relatively
460 increased when tremor was present, especially during tremor onset (1.20–1.66 fold, $p \leq 0.016$, Kruskal-
461

462 Wallis test, $p < 0.05$, Conover test) (**Figure 3B**). Furthermore, MC-tremor θ PLV increased from
463 no-tremor to tremor-onset to sustained-tremor ($p = 9.55 \times 10^{-37}$, Kruskal-Wallis test, $p < 0.05$, Conover
464 test) (**Figure 4A**). Interestingly, examining the PSI for MC θ and tremor revealed that MC θ led tremor
465 during both tremor onset and sustained tremor ($p \leq 0.014$, bootstrap test) (**Figure 4B**). Thus, in
466 contrast to SC, MC θ preceded tremor output.

467

468 Tremor-related θ transitioned from STN to cortex during tremor onset

469 Because both STN and MC θ power were elevated during tremor onset, and STN and MC θ phase led
470 tremor phase during tremor onset, we investigated the dynamics of STN-MC coupling during the dy-
471 namics of tremor initiation. Static phase slope analysis of STN and MC revealed that STN θ led MC θ
472 during tremor onset ($p < 0.001$, bootstrap test) (**Figure 5A**). To understand if this phase relationship
473 was time-locked to increasing tremor, we calculated STN-MC θ PSI as a function of time within the
474 tremor onset window. Within this epoch, STN θ preceded MC θ most consistently about 0.5 seconds
475 after tremor detection ($t = 0$) to the end of the tremor onset epoch ($t = 0.5$ – 1.0 seconds; $p < 0.05$,
476 bootstrap test) (**Figure 5B**). At no point in this window did MC θ appear to precede STN θ .

477 We also investigated whether STN θ and MC θ power influenced each other by calculating time-varying
478 nonparametric spectral granger prediction (GP) (see *Methods*). Briefly, a nonzero GP at a particular
479 frequency indicated that spectral power in one structure was predictive of spectral power in another.
480 Unlike the PSI, GP allows the disentangling of asymmetric, bidirectional influences across two signals
481 (Dhamala et al., 2008). As with PSI, STN θ power predicted MC θ power from 200 ms after the tremor
482 onset trigger to the end of epoch ($t = 0.2$ – 1.0 seconds; $p < 0.05$, bootstrap test) (**Figure 5C**). Again,
483 MC θ did not predict STN θ at any point in the epoch. Together, these results converged to suggest STN
484 θ drove MC θ during tremor onset.

485 Once tremor was established however, the θ phase slope relationship flipped, with MC θ phase preced-
486 ing STN θ phase (**Figure 5A**), revealing a dynamic transition with increasing tremor. Taken together
487 with the loss of STN θ influence over tremor during sustained tremor (**Figure 4B**), tremor output
488 appeared to become cortically rather than STN driven as tremor became established.

489 Because the STN and SC both exhibited positive correlations between θ power and increasing tremor,
490 we also investigated whether STN/SC dynamics varied during tremor onset. Like MC, static phase slope
491 analysis of STN and SC θ revealed that STN θ led SC during tremor onset ($p < 0.001$, bootstrap test)
492 (**Figure 5D**). Dynamic STN-SC PSI additionally revealed that STN θ led SC θ between 200 ms after
493 the tremor onset trigger to the end of the epoch ($t = 0.2$ – 1.0 seconds; $p < 0.001$, bootstrap test) (**Figure**
494 **5E**). Simultaneously, STN θ power predicted SC θ power from 400 ms before the tremor onset trigger to
495 end of the tremor onset epoch ($t = -0.4$ – $+1.0$ seconds; $p < 0.001$, bootstrap test) (**Figure 5F**). During

496 sustained tremor epochs however, the θ phase slope relationship between STN and SC became ambiguous
497 ($p = 0.091$, bootstrap test), again representing a loss of STN influence over cortical θ activity (**Figure**
498 **5D**). Altogether, although the STN drove both tremor and cortical θ as tremor emerged, the transition
499 to sustained tremor was accompanied by a decoupling of the STN from cortex in the θ band (**Figure 5G**).

500

501 **Motor cortex decoupled from posterior cortices with increasing tremor**

502 As STN-MC θ phase influence flipped from tremor onset to sustained tremor, we investigated whether
503 the functional connectivity of MC extended to other cortical regions with increasing tremor. To un-
504 derstand if tremor-mediated cortico-cortical interactions occurred in frequency bands other than θ , we
505 calculated both nondirected (PLV) and directed (GP) functional connectivity between the MC and other
506 cortical regions across the 3–100 Hz spectrum. While MC-SC PLV was broadly modulated by tremor
507 state ($p \leq 1.81 \times 10^{-66}$, Kruskal-Wallis test), it specifically decreased across all bands except γ_{mid}
508 during tremor onset (PLV, 1.20–7.72 fold decrease, $p < 0.05$, Conover test) (**Figure 6A**). To identify
509 whether synchrony detected by the PLV was driven by one structure in the pair, broad-spectrum GP was
510 calculated. However, no consistent band-wide differences in MC-SC GP were found across tremor states
511 ($p > 0.05$, bootstrap) (**Figure 6B**).

512 MC-PPC PLV similarly decreased across all frequencies except γ_{mid} as tremor increased (PLV, 1.07–
513 2.95 fold decrease, $p \leq 1.13 \times 10^{-20}$, Kruskal-Wallis test, $p < 0.05$, Conover test) (**Figure 6A**). Despite
514 this drop, the MC-PPC PLV spectrum revealed coupling peaks in α and $\beta_{high}/\gamma_{low}$ (20–60 Hz) frequencies
515 across all tremor states. However, each peak appeared as a directed channel of communication across MC
516 and PPC, particularly in the absence of tremor. Granger analysis revealed that while PPC α predicted
517 MC α regardless of tremor state, (GP, 0.94–5.24 fold difference, $p < 0.001$, bootstrap test in all tremor
518 states), its absolute prediction was 3.25 fold smaller in sustained tremor vs. no tremor (**Figure 6B**). In
519 contrast, MC $\beta_{high}/\gamma_{low}$ predicted PPC $\beta_{high}/\gamma_{low}$ exclusively in the absence of tremor (GP, 0.93–1.93
520 fold difference, $p < 0.001$, bootstrap test).

521 In sum, MC became less coupled with posterior cortical regions (SC, PPC) with increasing tremor,
522 while MC became increasingly coupled with PMC. Specifically, MC-PMC PLV increased within θ/α (6–10
523 Hz) specifically during sustained tremor (PLV, 1.54–3.67 fold increase, $p \leq 1.80 \times 10^{-152}$, Kruskal-Wallis
524 test, $p < 0.05$, Conover test) (**Figure 6A**). While not entirely within the same frequency range, PMC
525 θ appeared to predict MC θ during sustained tremor (GP, 1.86–7.28 fold increase, $p < 0.001$, bootstrap
526 test) (**Figure 6B**).

527

528 **Premotor cortex coupled with posterior cortices during tremor**

529 Because SC decoupled from the STN during sustained tremor while still reflecting tremor output, we

530 investigated whether SC instead coupled with other cortical regions as tremor increased. SC and PPC
531 exhibited increased θ/α (6–12 Hz) PLV (PLV, 1.02–1.16 fold increase, $p \leq 4.62 \times 10^{-39}$, Kruskal-Wallis
532 test, $p < 0.05$, Conover test) and decreased $\beta_{high-\gamma}$ (20–100 Hz) PLV (PLV, 1.10–1.38 fold decrease,
533 $p \leq 1.71 \times 10^{-91}$, Kruskal-Wallis test, $p < 0.05$, Conover test) with increasing tremor (**Figure 6C**).
534 While SC-PPC functional connectivity was relatively symmetric during low-tremor states (no tremor,
535 tremor onset), sustained tremor revealed more directed coupling. Although β_{low} PLV did not signifi-
536 cantly modulate with tremor, α/β_{low} (8–20 Hz) SC–PPC PLV during sustained tremor was driven by
537 PPC (GP, 1.65–20.85 fold difference, $p < 0.001$, bootstrap test) (**Figure 6D**). Additionally, PPC θ
538 predicted SC θ during sustained tremor (GP, 1.73–2.80 fold difference, $p < 0.001$, bootstrap test). Thus,
539 SC-PPC functional connectivity shifted to a distinct state during sustained tremor, with PPC predicting
540 lower frequencies (θ , α , β_{low}) in SC. At the same time, higher frequency (γ) coupling between SC and
541 PPC decreased as tremor increased.

542 SC and PMC interactions also exhibited push-pull changes in functional connectivity, with increased
543 β_{low} PLV (PLV, 1.04–1.09 fold increase, $p \leq 6.43 \times 10^{-33}$, Kruskal-Wallis test, $p < 0.05$, Conover test)
544 and decreased γ PLV (PLV, 1.42–2.19 fold decrease, $p \leq 1.32 \times 10^{-309}$, Kruskal-Wallis test, $p < 0.05$,
545 Conover test) with increasing tremor (**Figure 6C**). Like PPC, increases in lower frequency PLV (β_{low})
546 was driven by PMC specifically during sustained tremor (GP, 4.35–12.26 fold difference, $p < 0.001$,
547 bootstrap test) (**Figure 6D**).

548 Thus, in contrast to MC, which broadly decoupled from posterior cortical regions, SC became increas-
549 ingly coupled with and influenced by both posterior (PPC) and anterior (PMC) cortices with increasing
550 tremor. However, this increase in connectivity was specific to α/β_{low} frequencies while γ coupling de-
551 creased between SC and PMC/PPC.

552 To follow the spread of tremor-related cortical coupling, we investigated whether PMC and PPC
553 interacted during sustained tremor. Here, we observed an exaggerated version of the same tremor-
554 induced frequency shift (γ to β) of power and phase synchrony. When analyzing tremor epoch-related
555 spectral power in PMC and PPC in **Figure 3B**, both regions demonstrated tremor-related increases in
556 α/β_{low} power (PPC : 1.09–1.94 fold increase, $p \leq 3.88 \times 10^{-29}$, Kruskal-Wallis test, $p < 0.05$, Conover
557 test) (PMC: 1.07–2.21 fold increase, $p \leq 4.08 \times 10^{-14}$, Kruskal-Wallis test, $p < 0.05$, Conover test). At
558 the same time PMC and PPC exhibited decreases in γ_{mid} , γ_{high} , and hfo power relative to no tremor
559 (PMC: 1.22–5.42 fold decrease, $p \leq 1.20 \times 10^{-57}$, Kruskal-Wallis test, $p < 0.05$, Conover test) (PPC :
560 1.67–7.78 fold decrease, $p \leq 0.011$, Kruskal-Wallis test, $p < 0.05$, Conover test).

561 These similar changes in power were mirrored by changes in PMC-PPC PLV synchrony (**Figure**
562 **6C**). PMC-PPC $\gamma_{low-mid}$ PLV decreased as tremor increased (PLV, 1.06–6.59 fold decrease, $p \leq$
563 1.02×10^{-232} , Kruskal-Wallis test, $p < 0.05$, Conover test), while PMC-PPC β_{low} PLV increased with

564 tremor (PLV, 1.15–1.53 fold increase, $p \leq 8.34 \times 10^{-173}$, Kruskal-Wallis test, $p < 0.05$, Conover test).
565 Regardless of tremor state, PMC-PPC phase synchrony was driven by PMC onto PPC. When tremor
566 was absent, PMC γ predicted PPC γ (GP, 0.94–3.31 fold difference, $p < 0.001$, bootstrap test) (**Figure**
567 **6D**). During sustained tremor, PMC β power predicted PPC β power (GP, 1.76–12.14 fold difference,
568 $p < 0.001$, bootstrap test).

569 Overall, tremor was associated with a frequency shift (γ to β) of power and phase synchrony between
570 PMC, PPC, and SC. Specifically, PMC exerted increasing influence over posterior regions (SC, PPC) in
571 lower frequencies (α , β_{low}) with increasing tremor. However, this increase in lower frequency coupling
572 coincided with decreases in higher frequency coupling (γ). In addition, γ coupling between MC and PPC
573 decreased with increasing tremor, revealing that sustained tremor is a state of decreased γ synchrony
574 across sensorimotor cortex.

575

576 DISCUSSION

577 Using a naturalistic behavioral task, we were able to characterize tremor dynamics and isolate specific
578 tremor states, particularly tremor onset and maintenance. Across structures we found that θ power posi-
579 tively and β power negatively correlated with tremor, as has been found in previous reports (Hirschmann
580 et al., 2013; Qasim et al., 2016; Asch et al., 2020). However, our study is the first to dissect electrophys-
581 iological correlates of tremor onset and sustained tremor. During the emergence of tremor, not only did
582 STN and motor cortical θ power increase, but STN and motor cortical θ phase preceded the phase of
583 tremor. Moreover, STN θ activity drove motor cortical θ during tremor onset, suggesting a direct role of
584 the STN in initiating tremor output.

585 Once tremor emerged however, motor cortex appeared to sustain tremor. At the same time, motor
586 cortex became less coupled with somatosensory and parietal cortices, despite the presence of prominent
587 somatosensory cortex θ power which closely followed tremor. Instead, premotor cortex synchronized via
588 β_{low} frequencies with posterior cortices (somatosensory, parietal) at the expense of γ frequency synchro-
589 nization observed in the absence of tremor. This β_{low} synchrony was notably asymmetric across these
590 structures, with premotor cortex exerting influence over posterior cortices.

591 Taken together, although tremor amplitude corresponded to global changes in θ and β power, the
592 relationship between these frequency bands to tremor output was highly structure-specific. While STN-
593 motor cortical interactions appeared to initiate tremor, premotor cortex-driven network effects may help
594 sustain tremor. This STN-mediated dynamic reorganization of cortical connectivity is consistent with
595 both the “dimmer switch” model and the “intrinsic” and “extrinsic” cortical loops of Parkinson’s tremor
596 (Helmich et al., 2011; Volkmann et al., 1996) (**Figure 7**). Like the GPi, we revealed that the STN acted
597 as a “switch” to mediate the onset of tremor by influencing motor cortex (Dirkx et al., 2016). While

598 these STN-motor cortical interactions formed the “intrinsic” loop of tremor output, we expanded this
599 model to reveal that shifts from γ to β synchrony across premotor-parietal cortices potentially acted as
600 the “extrinsic” loop to stabilize the tremor state.

601

602 **Tremor onset was mediated by subthalamic θ driving motor cortex**

603 STN θ amplitude positively correlated with tremor amplitude regardless of tremor dynamic states. While
604 the phase of STN θ consistently preceded tremor phase during tremor onset, it did not during sustained
605 tremor. However, STN θ activity was still significantly phase-locked to tremor during sustained tremor.
606 This mixed relationship to tremor may reflect several roles of STN: interconnections with GPi contribute
607 to tremor initiation, while disynaptic connections with cerebellum may influence ongoing monitoring of
608 tremor output (Helmich et al., 2011; Bostan et al., 2010).

609 Regardless, STN θ drove motor cortex activity during tremor onset. While tremor has previously
610 been found to decrease β coherence between STN and motor cortex (Qasim et al., 2016) while increasing
611 θ coherence (Hirschmann et al., 2013), we demonstrated directed θ phase interactions from STN to motor
612 cortex specifically during tremor onset. While a previous case study of tremor onset displayed local STN
613 and cortical α/β power changes with tremor onset (Hirschmann et al., 2019), we show here that STN and
614 motor cortical θ activity are directionally linked. We also demonstrated that during sustained tremor, the
615 STN-motor cortex θ phase slope relationship reversed, suggesting the θ influence over sustained tremor
616 shifted source from STN to cortex.

617

618 **Motor cortex desynchronized with posterior cortices while sustaining tremor**

619 As tremor progressed, motor cortex θ increasingly drove tremor. While previous studies have correlated
620 motor cortical activity to tremor (Helmich et al., 2011; Timmermann et al., 2003), this is the first study
621 to our knowledge that has demonstrated a directed relationship between ECoG recordings and tremor.
622 Although motor cortex was synchronized to tremor, motor cortex appeared to desynchronize with other
623 cortical structures with the exception of premotor cortex, as has been found previously (Timmermann et
624 al., 2003; Qasim et al., 2016). While other studies have found that motor cortex increased its synchrony
625 with premotor and parietal cortices during tremor (Hirschmann et al., 2013), this was calculated only at
626 tremor and double-tremor frequencies.

627

628 **Tremor reorganized premotor and parietal cortical coupling**

629 Although premotor and parietal cortices did not exhibit a direct θ relationship to tremor, changes in
630 tremor initiated a frequency shift in premotor-parietal coupling dynamics. In the absence of tremor,
631 these regions were functionally coupled at higher frequencies (β_{high} , $\gamma_{low-mid}$). fMRI studies in patients

632 with PD have found that these regions exhibit overactive BOLD activity during self-initiated sequential
633 hand movements (Samuel et al., 1997), which is hypothesized to compensate for decreased BOLD activ-
634 ity in fronto-striatal circuits in the dopamine depleted state (Wu et al., 2011). Furthermore, cortical γ
635 frequency power and synchrony are associated specifically with voluntary movement (Crone et al., 1998;
636 Miller et al., 2007). In our study, this bidirectional premotor-parietal γ activity may have reflected task
637 monitoring and spatial tracking (motor output) using sensory information.

638 During sustained tremor however, parietal and premotor cortices both exhibited increases in β_{low}
639 power. This β_{low} activity was also functionally coupled, with premotor driving parietal cortex. Elevated
640 β_{low} oscillations have been observed in premotor cortex recordings in MPTP non-human primates with
641 predominantly akinetic/rigid symptoms (Wang et al., 2017). While not observed in our study, increased
642 premotor β_{high} influence over the STN has also been found to correlate with akinetic/rigid symptoms
643 (Sharott et al., 2018). Premotor β_{low} oscillations may function here in a similar anti-kinetic fashion with
644 other cortical structures during tremor.

645 In any case, with increasing tremor premotor-parietal γ activity diminished while premotor β_{low}
646 activity drove parietal activity. These frequency shifts may be best understood in the framework of
647 communication-through-coherence theory (Fries, 2015). Specifically, while symmetric or bottom-up γ os-
648 cillations permit effective and precise transmission of motor-related information across structures, lower-
649 frequency oscillations such as α/β act as top-down feedback. Here, task-related γ synchrony observed
650 across sensorimotor cortex decreased with tremor. In contrast, lower-frequency oscillations such as β_{low}
651 increased in synchrony, perhaps acting as pathological “feedback” restricting further voluntary move-
652 ment. Thus, voluntary movement which normally acts to suppress tremor is impeded (Naros et al.,
653 2018). As motor cortical-thalamo-cerebellar loops have been found to sustain and modulate tremor am-
654 plitude (Dirkx et al., 2016), our results extend this model by showing premotor α/β_{low} activity may
655 suppress voluntary movement, allowing tremor to persist.

656

657 **Implications for closed-loop deep brain stimulation**

658 Because of the clinical interest in developing adaptive closed-loop DBS to more precisely treat PD symp-
659 toms, various electrophysiological observations have been investigated as potential tremor biomarkers to
660 inform stimulation (Hirschmann et al., 2017; Shah et al., 2018; Yao et al., 2020). While promising, the
661 features used for tremor detection do not take into account the dynamic nature of tremor — namely,
662 the distinct neurophysiological signature of tremor onset. Because of the breadth of STN β -frequency
663 oscillation research in PD, initial closed-loop DBS efforts have focused on using β oscillations as a proxy
664 for bradykinesia symptoms (Little et al., 2013; Little et al., 2016; Little et al., 2016; Velisar et al., 2019).
665 However, β -driven DBS has been shown to worsen tremor in some patients (Pia-Fuentes et al., 2020;

666 He et al., 2020).

667 Here, we demonstrated that subthalamic θ was present whether tremor was emerging or sustained.
668 The addition of STN θ -based biomarkers to closed-loop DBS could help treat the separate symptom axis
669 of tremor. Further, we have provided the best evidence to date that cortical ECoG θ is a robust marker
670 for tremor. Specifically, we found that motor cortical θ was synchronized to STN θ during tremor states,
671 and that somatosensory θ was a reliable indicator of immediate tremor amplitude.

672 These results overall argue for a combined subcortical-cortical stimulation/recording paradigm not
673 unlike cortical-thalamic closed-loop DBS for ET (Opri et al., 2020). By combining recordings from the
674 STN and sensorimotor cortex, an algorithm could infer whether tremor was about to emerge (STN and
675 MC θ) or was already present (SC θ). In particular, somatosensory cortical recordings could allow for con-
676 tinuous monitoring of tremor despite any stimulus artifact or competing oscillations in the STN. Ideally,
677 DBS for a patient with a mixed motor phenotype could be optimized between STN β for bradykinesia
678 symptoms and SC θ oscillations for tremor.

679

680 **Limitations and Conclusions**

681 Because all tremor data were quantified from patients as they were moving their upper limb during
682 our tracking task, our tremor conditions do not reflect a pure “rest” tremor. However, as Parkinsonian
683 tremor can often emerge as patients maintain a posture or perform a task, our approach still captured
684 meaningful aspects of tremor. Due to our PD population receiving mostly STN DBS for clinical reasons,
685 we were unable to assess the role of the GPi and motor thalamus (VIM) neurophysiology to tremor onset
686 and/or maintenance. Nevertheless, our awake behaving intraoperative recordings revealed that the STN
687 and motor cortex work together to initiate tremor, and tremor is in part sustained by premotor-parietal
688 synchrony.

689 REFERENCES

- 690 Accolla E, Caputo E, Cogiamanian F, Tamma F, MrakicSposta S, Marceglia S, Egidì M,
691 Rampini P, Locatelli M, Priori A (2007) Gender differences in patients with Parkinson’s dis-
692 ease treated with subthalamic deep brain stimulation. *Movement Disorders* 22:1150–1156 .eprint:
693 <https://onlinelibrary.wiley.com/doi/pdf/10.1002/mds.21520>.
- 694 Akbar U, Asaad WF (2017) A Comprehensive Approach to Deep Brain Stimulation for Movement
695 Disorders. *Rhode Island Medical Journal (2013)* 100:30–33.
- 696 Albin RL, Young AB, Penney JB (1989) The functional anatomy of basal ganglia disorders. *Trends in*
697 *Neurosciences* 12:366–375.
- 698 Argall BD, Saad ZS, Beauchamp MS (2006) Simplified intersubject averaging
699 on the cortical surface using SUMA. *Human Brain Mapping* 27:14–27 .eprint:
700 <https://onlinelibrary.wiley.com/doi/pdf/10.1002/hbm.20158>.
- 701 Asaad WF, Eskandar EN (2008a) Achieving behavioral control with millisecond resolution in a high-level
702 programming environment. *Journal of neuroscience methods* 173:235–240.
- 703 Asaad WF, Eskandar EN (2008b) A flexible software tool for temporally-precise behavioral control in
704 Matlab. *Journal of neuroscience methods* 174:245–258.
- 705 Asaad WF, Santhanam N, McClellan S, Freedman DJ (2013) High-performance execution of psy-
706 chophysical tasks with complex visual stimuli in MATLAB. *Journal of Neurophysiology* 109:249–260.
- 707 Asch N, Herschman Y, Maoz R, Aurbach-Asch C, Valsky D, Abu-Snineh M, Arkadir D, Linetsky E,
708 Eitan R, Marmor O, Bergman H, Israel Z (2020) Independently together: subthalamic theta and beta
709 opposite roles in predicting Parkinsons tremor. *Brain Communications* .
- 710 Aydore S, Pantazis D, Leahy RM (2013) A note on the phase locking value and its properties. *Neu-*
711 *roImage* 74:231–244.
- 712 Benjamini Y, Hochberg Y (1995) Controlling the False Discovery Rate: A Practical and Power-
713 ful Approach to Multiple Testing. *Journal of the Royal Statistical Society. Series B (Methodologi-*
714 *cal)* 57:289–300.
- 715 Bergman H, Wichmann T, Karmon B, DeLong MR (1994) The primate subthalamic nucleus. II. Neu-
716 ronal activity in the MPTP model of parkinsonism. *Journal of Neurophysiology* 72:507–520.

- 717 Bostan AC, Dum RP, Strick PL (2010) The basal ganglia communicate with the cerebellum. *Proceedings*
718 *of the National Academy of Sciences* 107:8452–8456 Publisher: National Academy of Sciences Section:
719 Biological Sciences.
- 720 Cagnan H, Little S, Foltynie T, Limousin P, Zrinzo L, Hariz M, Cheeran B, Fitzgerald J, Green
721 AL, Aziz T, Brown P (2014) The nature of tremor circuits in parkinsonian and essential tremor.
722 *Brain* 137:3223–3234.
- 723 Cox RW (1996) AFNI: Software for Analysis and Visualization of Functional Magnetic Resonance
724 Neuroimages. *Computers and Biomedical Research* 29:162–173.
- 725 Crone NE, Miglioretti DL, Gordon B, Lesser RP (1998) Functional mapping of human sensorimotor
726 cortex with electrocorticographic spectral analysis. II. Event-related synchronization in the gamma band.
727 *Brain* 121:2301–2315.
- 728 Dale AM, Fischl B, Sereno MI (1999) Cortical Surface-Based Analysis: I. Segmentation and Surface
729 Reconstruction. *NeuroImage* 9:179–194.
- 730 Desikan RS, Sgonne F, Fischl B, Quinn BT, Dickerson BC, Blacker D, Buckner RL, Dale AM, Maguire
731 RP, Hyman BT, Albert MS, Killiany RJ (2006) An automated labeling system for subdividing the
732 human cerebral cortex on MRI scans into gyral based regions of interest. *NeuroImage* 31:968–980.
- 733 Destrieux C, Fischl B, Dale A, Hagren E (2010) Automatic parcellation of human cortical gyri and
734 sulci using standard anatomical nomenclature. *NeuroImage* 53:1–15.
- 735 Dhamala M, Rangarajan G, Ding M (2008) Analyzing Information Flow in Brain Networks with Non-
736 parametric Granger Causality. *NeuroImage* 41:354–362.
- 737 Dirx MF, den Ouden HEM, Aarts E, Timmer MHM, Bloem BR, Toni I, Helmich RC (2017) Dopamine
738 controls Parkinsons tremor by inhibiting the cerebellar thalamus. *Brain* 140:721–734.
- 739 Dirx MF, Ouden Hd, Aarts E, Timmer M, Bloem BR, Toni I, Helmich RC (2016) The Cerebral Network
740 of Parkinson’s Tremor: An Effective Connectivity fMRI Study. *Journal of Neuroscience* 36:5362–5372
741 Publisher: Society for Neuroscience Section: Articles.
- 742 Dirx MF, Zach H, Bloem BR, Hallett M, Helmich RC (2018) The nature of postural tremor in Parkinson
743 disease. *Neurology* 90:e1095–e1103.
- 744 Dirx MF, Zach H, van Nuland A, Bloem BR, Toni I, Helmich RC (2019) Cerebral differences between
745 dopamine-resistant and dopamine-responsive Parkinsons tremor. *Brain* 142:3144–3157.

- 746 Fischl B, Salat DH, Busa E, Albert M, Dieterich M, Haselgrove C, van der Kouwe A, Killiany R,
747 Kennedy D, Klaveness S, Montillo A, Makris N, Rosen B, Dale AM (2002) Whole Brain Segmentation:
748 Automated Labeling of Neuroanatomical Structures in the Human Brain. *Neuron* 33:341–355.
- 749 Fonov V, Evans A, McKinstry R, Almlí C, Collins D (2009) Unbiased nonlinear average age-appropriate
750 brain templates from birth to adulthood. *NeuroImage* 47:S102.
- 751 Fries P (2015) Rhythms for Cognition: Communication through Coherence. *Neuron* 88:220–235.
- 752 Gross RE, Krack P, Rodriguez-Oroz MC, Rezai AR, Benabid AL (2006) Electrophysiological mapping
753 for the implantation of deep brain stimulators for Parkinson’s disease and tremor. *Movement Disorders:*
754 *Official Journal of the Movement Disorder Society* 21 Suppl 14:S259–283.
- 755 Hariz GM, Nakajima T, Limousin P, Foltynie T, Zrinzo L, Jahanshahi M, Hamberg K (2011) Gender
756 distribution of patients with Parkinsons disease treated with subthalamic deep brain stimulation; a
757 review of the 20002009 literature. *Parkinsonism & Related Disorders* 17:146–149.
- 758 Harris CR, Millman KJ, van der Walt SJ, Gommers R, Virtanen P, Cournapeau D, Wieser E, Taylor
759 J, Berg S, Smith NJ, Kern R, Picus M, Hoyer S, van Kerkwijk MH, Brett M, Haldane A, del Ro JF,
760 Wiebe M, Peterson P, Grard-Marchant P, Sheppard K, Reddy T, Weckesser W, Abbasi H, Gohlke C,
761 Oliphant TE (2020) Array programming with NumPy. *Nature* 585:357–362 Number: 7825 Publisher:
762 Nature Publishing Group.
- 763 He S, Mostofi A, Syed E, Torrecillos F, Tinkhauser G, Fischer P, Pogosyan A, Hasegawa H, Li Y,
764 Ashkan K, Pereira E, Brown P, Tan H (2020) Subthalamic beta targeted neurofeedback speeds up
765 movement initiation but increases tremor in Parkinsonian patients. *eLife* 9:e60979 Publisher: eLife
766 Sciences Publications, Ltd.
- 767 Helmich RC (2018) The cerebral basis of Parkinsonian tremor: A network perspective. *Movement*
768 *Disorders* 33:219–231.
- 769 Helmich RC, Hallett M, Deuschl G, Toni I, Bloem BR (2012) Cerebral causes and consequences of
770 parkinsonian resting tremor: a tale of two circuits? *Brain* 135:3206–3226.
- 771 Helmich RC, Janssen MJR, Oyen WJG, Bloem BR, Toni I (2011) Pallidal dysfunction drives a cerebel-
772 lothalamic circuit into Parkinson tremor. *Annals of Neurology* 69:269–281.
- 773 Hirschmann J, Schoffelen JM, Schnitzler A, van Gerven MAJ (2017) Parkinsonian rest tremor can
774 be detected accurately based on neuronal oscillations recorded from the subthalamic nucleus. *Clinical*
775 *Neurophysiology* 128:2029–2036.

- 776 Hirschmann J, Abbasi O, Storzer L, Butz M, Hartmann CJ, Wojtecki L, Schnitzler A (2019) Longitudinal
777 Recordings Reveal Transient Increase of Alpha/Low-Beta Power in the Subthalamic Nucleus Associated
778 With the Onset of Parkinsonian Rest Tremor. *Frontiers in Neurology* 10 Publisher: Frontiers.
- 779 Hirschmann J, Butz M, Hartmann CJ, Hoogenboom N, zkurt TE, Vesper J, Wojtecki L, Schnitzler
780 A (2016) Parkinsonian Rest Tremor Is Associated With Modulations of Subthalamic High-Frequency
781 Oscillations. *Movement Disorders* 31:1551–1559.
- 782 Hirschmann J, Hartmann CJ, Butz M, Hoogenboom N, zkurt TE, Elben S, Vesper J, Wojtecki L,
783 Schnitzler A (2013) A direct relationship between oscillatory subthalamic nucleus-cortex coupling and
784 rest tremor in Parkinson's disease. *Brain* 136:3659–3670.
- 785 Jankovic J, McDermott M, Carter J, Gauthier S, Goetz C, Golbe L, Huber S, Koller W, Olanow C,
786 Shoulson I (1990) Variable expression of Parkinson's disease: a base-line analysis of the DATATOP
787 cohort. The Parkinson Study Group. *Neurology* 40:1529–1534.
- 788 Koller WC (1984) The Diagnosis of Parkinson's Disease. *Archives of Internal Medicine* 144:2146–2147
789 Publisher: American Medical Association.
- 790 Koller WC (1986) Pharmacologic Treatment of Parkinsonian Tremor. *Archives of Neurology* 43:126–127
791 Publisher: American Medical Association.
- 792 Konrad PE, Neimat JS, Yu H, Kao CC, Remple MS, D'Haese PF, Dawant BM (2011) Customized,
793 miniature rapid-prototype stereotactic frames for use in deep brain stimulator surgery: initial clinical
794 methodology and experience from 263 patients from 2002 to 2008. *Stereotactic and Functional Neuro-*
795 *surgery* 89:34–41.
- 796 Lachaux JP, Rodriguez E, Martinerie J, Varela FJ (1999) Measuring phase synchrony in brain signals.
797 *Human Brain Mapping* 8:194–208.
- 798 Lance JW, Schwab RS, Peterson EA (1963) ACTION TREMOR AND THE COGWHEEL PHE-
799 NOMENON IN PARKINSONS DISEASE. *Brain* 86:95–110 Publisher: Oxford Academic.
- 800 Lauro PM, Lee S, Ahn M, Barborica A, Asaad WF (2018) DBStar: An Open-Source Tool Kit for Imag-
801 ing Analysis with Patient-Customized Deep Brain Stimulation Platforms. *Stereotactic and Functional*
802 *Neurosurgery* .
- 803 Lauro PM, Vanegas-Arroyave N, Huang L, Taylor PA, Zaghoul KA, Lungu C, Saad ZS, Horovitz SG
804 (2015) DBSproc: An open source process for DBS electrode localization and tractographic analysis.
805 *Human Brain Mapping* .

- 806 Levy R, Hutchison WD, Lozano AM, Dostrovsky JO (2000) High-frequency Synchronization of Neu-
807 ronral Activity in the Subthalamic Nucleus of Parkinsonian Patients with Limb Tremor. *Journal of*
808 *Neuroscience* 20:7766–7775.
- 809 Li X, Morgan PS, Ashburner J, Smith J, Rorden C (2016) The first step for neuroimaging data analysis:
810 DICOM to NIfTI conversion. *Journal of Neuroscience Methods* 264:47–56.
- 811 Little S, Beudel M, Zrinzo L, Foltynie T, Limousin P, Hariz M, Neal S, Cheeran B, Cagnan H, Gratwicke
812 J, Aziz TZ, Pogosyan A, Brown P (2016) Bilateral adaptive deep brain stimulation is effective in
813 Parkinson’s disease. *Journal of Neurology, Neurosurgery, and Psychiatry* 87:717–721.
- 814 Little S, Pogosyan A, Neal S, Zavala B, Zrinzo L, Hariz M, Foltynie T, Limousin P, Ashkan K, FitzGerald
815 J, Green AL, Aziz TZ, Brown P (2013) Adaptive deep brain stimulation in advanced Parkinson disease.
816 *Annals of Neurology* 74:449–457.
- 817 Little S, Tripoliti E, Beudel M, Pogosyan A, Cagnan H, Herz D, Bestmann S, Aziz T, Cheeran B,
818 Zrinzo L, Hariz M, Hyam J, Limousin P, Foltynie T, Brown P (2016) Adaptive deep brain stimulation
819 for Parkinson’s disease demonstrates reduced speech side effects compared to conventional stimulation
820 in the acute setting. *Journal of Neurology, Neurosurgery, and Psychiatry* 87:1388–1389.
- 821 Liu Y, Coon WG, Pesterev Ad, Brunner P, Schalk G (2015) The effects of spatial filtering and artifacts
822 on electrocorticographic signals. *Journal of Neural Engineering* 12:056008 Publisher: IOP Publishing.
- 823 Miller KJ, Leuthardt EC, Schalk G, Rao RPN, Anderson NR, Moran DW, Miller JW, Ojemann JG
824 (2007) Spectral Changes in Cortical Surface Potentials during Motor Movement. *Journal of Neuro-*
825 *science* 27:2424–2432.
- 826 Naros G, Grimm F, Weiss D, Gharabaghi A (2018) Directional communication during movement
827 execution interferes with tremor in Parkinson’s disease. *Movement Disorders* 33:251–261 .eprint:
828 <https://onlinelibrary.wiley.com/doi/pdf/10.1002/mds.27221>.
- 829 Nolte G, Ziehe A, Nikulin VV, Schlgl A, Krmer N, Brismar T, Mller KR (2008) Robustly Estimating
830 the Flow Direction of Information in Complex Physical Systems. *Physical Review Letters* 100:234101
831 Publisher: American Physical Society.
- 832 Opri E, Cerner S, Molina R, Eisinger RS, Cagle JN, Almeida L, Denison T, Okun MS, Foote KD,
833 Gunduz A (2020) Chronic embedded cortico-thalamic closed-loop deep brain stimulation for the treat-
834 ment of essential tremor. *Science Translational Medicine* 12 Publisher: American Association for the
835 Advancement of Science Section: Research Article.

- 836 Pia-Fuentes D, van Dijk JMC, van Zijl JC, Moes HR, van Laar T, Oterdoom DLM, Little S, Brown
837 P, Beudel M (2020) Acute effects of Adaptive Deep Brain Stimulation in Parkinsons disease. *Brain*
838 *Stimulation* .
- 839 Prerau MJ, Brown RE, Bianchi MT, Ellenbogen JM, Purdon PL (2016) Sleep Neurophysiological
840 Dynamics Through the Lens of Multitaper Spectral Analysis. *Physiology* 32:60–92 Publisher: American
841 Physiological Society.
- 842 Qasim SE, de Hemptinne C, Swann NC, Miocinovic S, Ostrem JL, Starr PA (2016) Electrocorticogra-
843 phy reveals beta desynchronization in the basal ganglia-cortical loop during rest tremor in Parkinson’s
844 disease. *Neurobiology of Disease* 86:177–186.
- 845 Raz A, Vaadia E, Bergman H (2000) Firing Patterns and Correlations of Spontaneous Discharge of
846 Pallidal Neurons in the Normal and the Tremulous 1-Methyl-4-Phenyl-1,2,3,6-Tetrahydropyridine Vervet
847 Model of Parkinsonism. *Journal of Neuroscience* 20:8559–8571 Publisher: Society for Neuroscience
848 Section: ARTICLE.
- 849 Reck C, Florin E, Wojtecki L, Krause H, Groiss S, Voges J, Maarouf M, Sturm V, Schnitzler A, Timmer-
850 mann L (2009) Characterisation of tremor-associated local field potentials in the subthalamic nucleus
851 in Parkinsons disease. *European Journal of Neuroscience* 29:599–612.
- 852 Reck C, Himmel M, Florin E, Maarouf M, Sturm V, Wojtecki L, Schnitzler A, Fink GR, Timmermann L
853 (2010) Coherence analysis of local field potentials in the subthalamic nucleus: differences in parkinsonian
854 rest and postural tremor. *European Journal of Neuroscience* 32:1202–1214.
- 855 Rumalla K, Smith KA, Follett KA, Nazzaro JM, Arnold PM (2018) Rates, causes, risk factors, and
856 outcomes of readmission following deep brain stimulation for movement disorders: Analysis of the U.S.
857 Nationwide Readmissions Database. *Clinical Neurology and Neurosurgery* 171:129–134.
- 858 Saad ZS, Reynolds RC (2012) SUMA. *NeuroImage* 62:768–773.
- 859 Samuel M, Ceballos-Baumann AO, Blin J, Uema T, Boecker H, Passingham RE, Brooks DJ (1997)
860 Evidence for lateral premotor and parietal overactivity in Parkinson’s disease during sequential and
861 bimanual movements. A PET study. *Brain* 120:963–976 Publisher: Oxford Academic.
- 862 Shah SA, Tinkhauser G, Chen CC, Little S, Brown P (2018) Parkinsonian Tremor Detection from
863 Subthalamic Nucleus Local Field Potentials for Closed-Loop Deep Brain Stimulation. *Conference pro-*
864 *ceedings: ... Annual International Conference of the IEEE Engineering in Medicine and Biology Society.*
865 *IEEE Engineering in Medicine and Biology Society. Annual Conference* 2018:2320–2324.

- 866 Sharott A, Gulberti A, Hamel W, Kppen JA, Mnchau A, Buhmann C, Ptter-Nerger M, Westphal M,
867 Gerloff C, Moll CKE, Engel AK (2018) Spatio-temporal dynamics of cortical drive to human subthalamic
868 nucleus neurons in Parkinson’s disease. *Neurobiology of Disease* 112:49–62.
- 869 Telkes I, Viswanathan A, Jimenez-Shahed J, Abosch A, Ozturk M, Gupte A, Jankovic J, Ince NF
870 (2018) Local field potentials of subthalamic nucleus contain electrophysiological footprints of motor
871 subtypes of Parkinson’s disease. *Proceedings of the National Academy of Sciences of the United States*
872 *of America* 115:E8567–E8576.
- 873 Terpilowski M (2019) scikit-posthocs: Pairwise multiple comparison tests in Python. *Journal of Open*
874 *Source Software* 4:1169.
- 875 Timmermann L, Gross J, Dirks M, Volkmann J, Freund HJ, Schnitzler A (2003) The cerebral oscillatory
876 network of parkinsonian resting tremor. *Brain* 126:199–212.
- 877 Trotta MS, Cocjin J, Whitehead E, Damera S, Wittig JH, Saad ZS, Inati SK, Zaghoul KA (2018)
878 Surface based electrode localization and standardized regions of interest for intracranial EEG. *Human*
879 *Brain Mapping* 39:709–721.
- 880 Velisar A, Syrkin-Nikolau J, Blumenfeld Z, Trager MH, Afzal MF, Prabhakar V, Bronte-Stewart H
881 (2019) Dual threshold neural closed loop deep brain stimulation in Parkinson disease patients. *Brain*
882 *Stimulation* .
- 883 Vinck M, van Wingerden M, Womelsdorf T, Fries P, Pennartz CMA (2010) The pairwise phase consis-
884 tency: A bias-free measure of rhythmic neuronal synchronization. *NeuroImage* 51:112–122.
- 885 Virtanen P, Gommers R, Oliphant TE, Haberland M, Reddy T, Cournapeau D, Burovski E, Peterson P,
886 Weckesser W, Bright J, Walt SJvd, Brett M, Wilson J, Millman KJ, Mayorov N, Nelson ARJ, Jones E,
887 Kern R, Larson E, Carey CJ, Polat , Feng Y, Moore EW, VanderPlas J, Laxalde D, Perktold J, Cimrman
888 R, Henriksen I, Quintero EA, Harris CR, Archibald AM, Ribeiro AH, Pedregosa F, Mulbregt Pv (2020)
889 SciPy 1.0: fundamental algorithms for scientific computing in Python. *Nature Methods* pp. 1–12.
- 890 Volkmann J, Joliot M, Mogilner A, Ioannides AA, Lado F, Fazzini E, Ribary U, Llinas R (1996) Cen-
891 tral motor loop oscillations in parkinsonian resting tremor revealed magnetoencephalography. *Neurol-*
892 *ogy* 46:1359–1359.
- 893 Wang J, Johnson LA, Jensen AL, Baker KB, Molnar GF, Johnson MD, Vitek JL (2017) Network-wide
894 oscillations in the parkinsonian state: alterations in neuronal activities occur in the premotor cortex
895 in parkinsonian nonhuman primates. *Journal of Neurophysiology* 117:2242–2249 Publisher: American
896 Physiological Society.

- 897 Wong JK, Viswanathan VT, Nozile-Firth KS, Eisinger RS, Leone EL, Desai AM, Foote KD, Ramirez-
898 Zamora A, Okun MS, Wagle Shukla A (2020) STN Versus GPi Ddeep Brain Stimulation for Action and
899 Rest Tremor in Parkinsons Disease. *Frontiers in Human Neuroscience* 14 Publisher: Frontiers.
- 900 Wu T, Wang L, Hallett M, Chen Y, Li K, Chan P (2011) Effective connectivity of brain networks during
901 self-initiated movement in Parkinson’s disease. *NeuroImage* 55:204–215.
- 902 Xiao Y, Beriault S, Pike GB, Collins DL (2012) Multicontrast multiecho FLASH MRI for targeting the
903 subthalamic nucleus. *Magnetic Resonance Imaging* 30:627–640.
- 904 Xiao Y, Fonov V, Briault S, Al Subaie F, Chakravarty MM, Sadikot AF, Pike GB, Collins DL (2015)
905 Multi-contrast unbiased MRI atlas of a Parkinson’s disease population. *International Journal of Com-
906 puter Assisted Radiology and Surgery* 10:329–341.
- 907 Xiao Y, Fonov V, Chakravarty MM, Beriault S, Al Subaie F, Sadikot A, Pike GB, Bertrand G, Collins
908 DL (2017) A dataset of multi-contrast population-averaged brain MRI atlases of a Parkinson’s disease
909 cohort. *Data in Brief* 12:370–379.
- 910 Yao L, Brown P, Shoaran M (2020) Improved detection of Parkinsonian resting tremor with feature
911 engineering and Kalman filtering. *Clinical Neurophysiology* 131:274–284.
- 912 Young CK, Ruan M, McNaughton N (2017) A Critical Assessment of Directed Connectivity Estimates
913 with Artificially Imposed Causality in the Supramammillary-Septo-Hippocampal Circuit. *Frontiers in
914 Systems Neuroscience* 11.
- 915 Zach H, Dirx M, Bloem BR, Helmich RC (2015) The Clinical Evaluation of Parkinsons Tremor. *Journal
916 of Parkinson’s Disease* 5:471–474 Publisher: IOS Press.

917 **FIGURE LEGENDS**

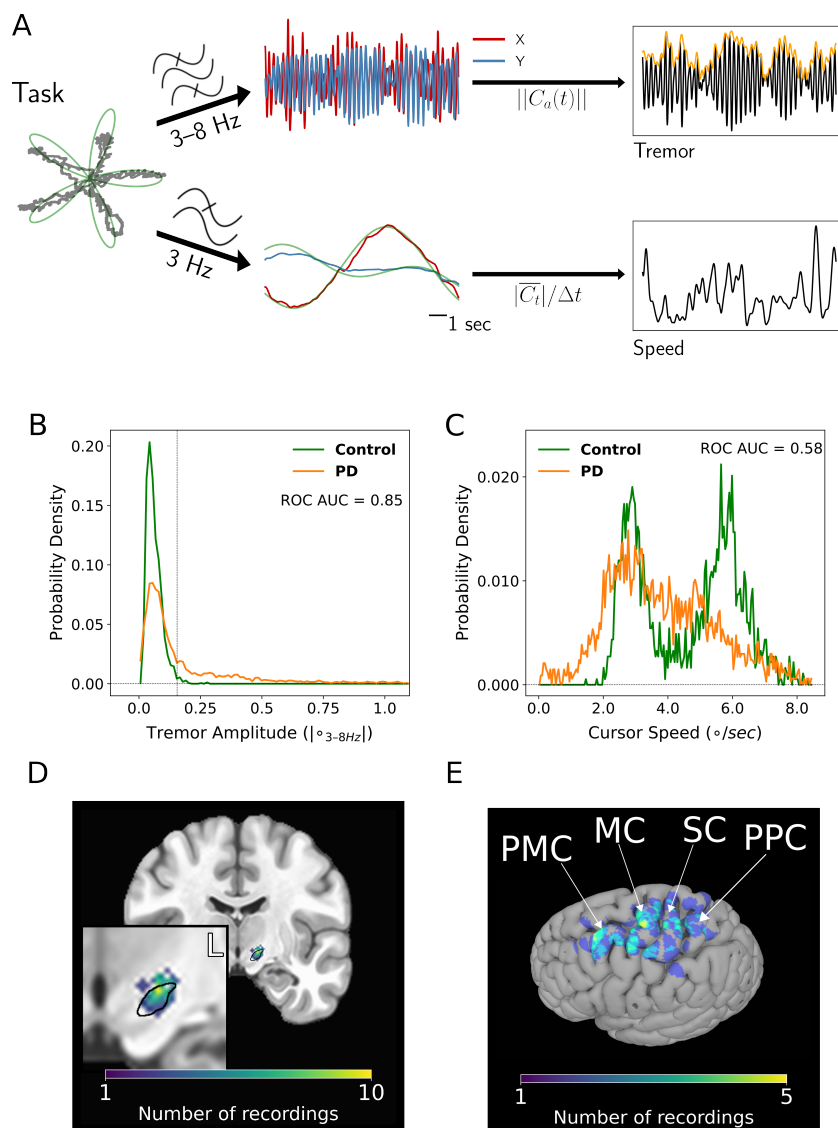


Figure 1. Tremor and movement speed calculated from the intraoperative visual-motor task.

A, Left - Schematic of task target (green) and joystick (gray) traces from a single trial. Center-top - Bandpass filtered X and Y joystick traces from the task trial. Center-bottom - Lowpass filtered X and Y joystick traces from the task trial. Right-top - One-dimensional projection of bandpass filtered traces (black), with tremor amplitude measured from the envelope (orange). Right-bottom - Cursor speed measured from lowpass filtered traces (black).

B, Distribution of 4 second tremor amplitude epochs for control subject and PD patient populations. \circ - degrees of visual angle. Vertical dashed line indicates ROC-derived cutoff value between control and PD populations. While there is overlap on the left side of the distribution (patients with PD can exhibit control-like performance), the PD distribution is highly skewed on the right side of the distribution, allowing a large range of tremor expression. ROC AUC - Receiver operator characteristic area under the curve.

C, Distribution of 4 second speed epochs for control subject and PD patient populations. The bimodality of the control distribution corresponded to the pre-programmed speed of the onscreen target. Despite this, note that the PD distribution is shifted towards lower speed values.

D, Coronal view of microelectrode recording density on an MNI reference volume. The inset panel displays a close-up view of the subthalamic nucleus (outlined in black). L - left.

E, Recording density of ECoG contacts on an MNI reference surface. PMC - premotor cortex; MC - motor cortex; SC - somatosensory cortex; PPC - parietal cortex.

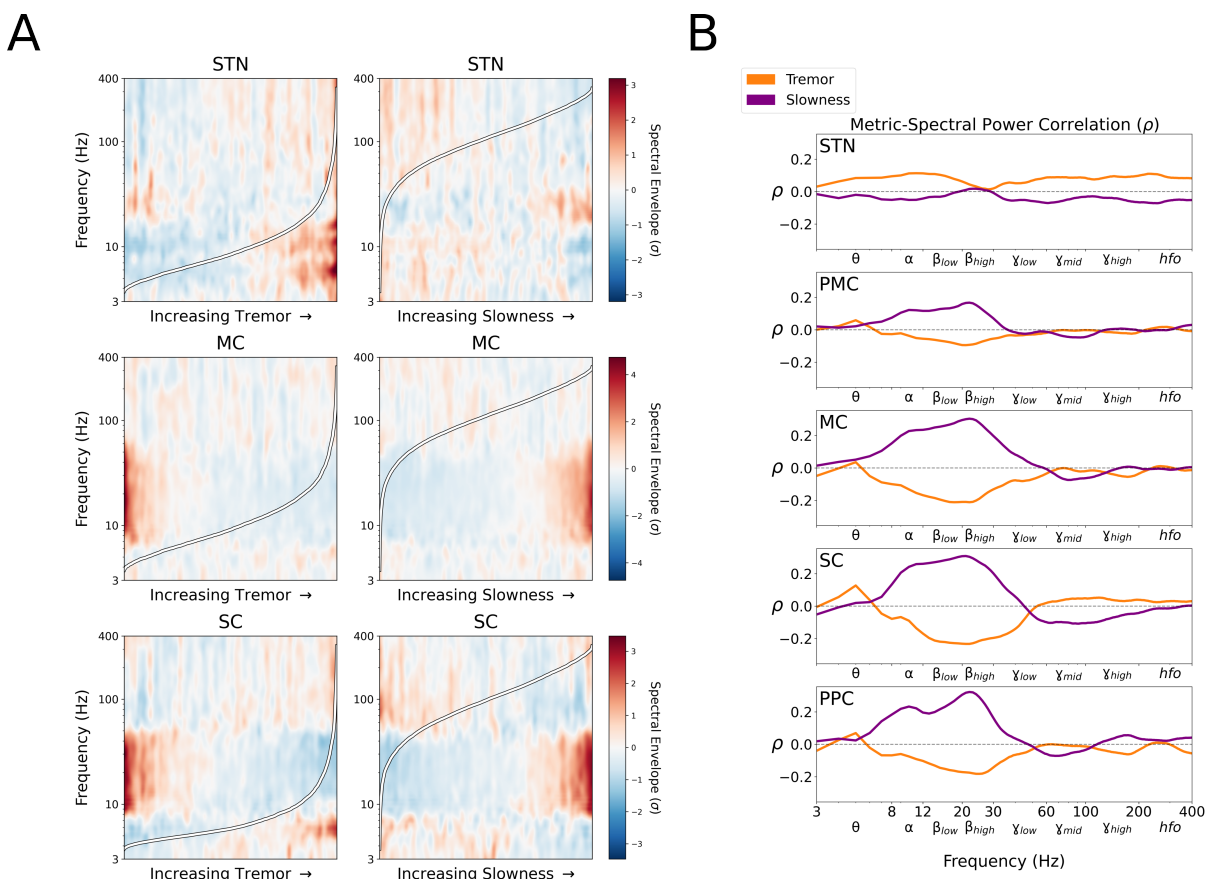


Figure 2. Tremor and slowness exhibit distinct spectral power correlations with intracranial recordings. **A**, Population-averaged task session spectral power, sorted by each epoch's tremor amplitude (left) or slowness (right). For ease of visualization, frequency power was Z-scored within frequencies across epochs. **B**, Average session-wide narrowband (1 Hz) spectral Spearman correlation (ρ) with tremor amplitude and slowness. Note that while β frequencies exhibited an opposing relationship with tremor and slowness, θ frequencies exhibited a distinct positive correlation with tremor. STN - subthalamic nucleus, PMC - premotor cortex; MC - motor cortex; SC - somatosensory cortex; PPC - parietal cortex.

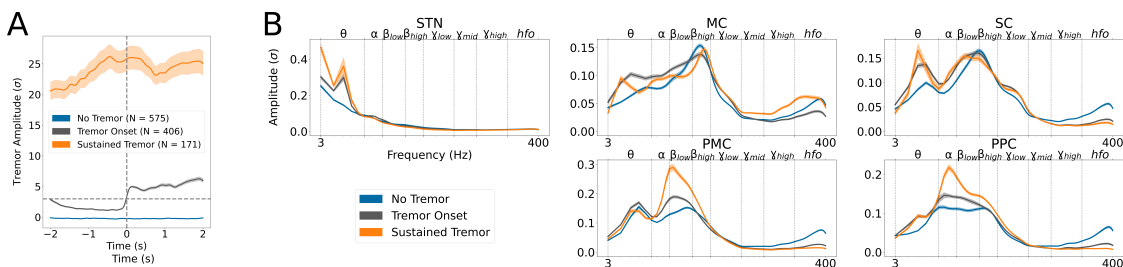


Figure 3. Spectral power during different tremor dynamic states.

A, Tremor event design. Based on a population-based tremor ROC threshold, epochs representing different states of tremor dynamics were isolated. For each event type, the average tremor amplitude (\pm standard error) in patients with PD relative to control subjects is displayed over time. Horizontal dashed line denotes the tremor threshold (3 standard deviations relative to control subjects). Vertical dashed line ($t = 0$) in tremor onset events represents the “trigger” where tremor amplitude crossed the tremor threshold.

B, Average spectral power (\pm standard error) across frequencies for each tremor event type, by recording site. Vertical dashed lines represent frequency band borders. While θ oscillations increased in power across STN, MC, and SC, increased tremor was associated with increased α/β_{low} power in PMC and PPC.

STN - subthalamic nucleus, PMC - premotor cortex; MC - motor cortex; SC - somatosensory cortex; PPC - parietal cortex.

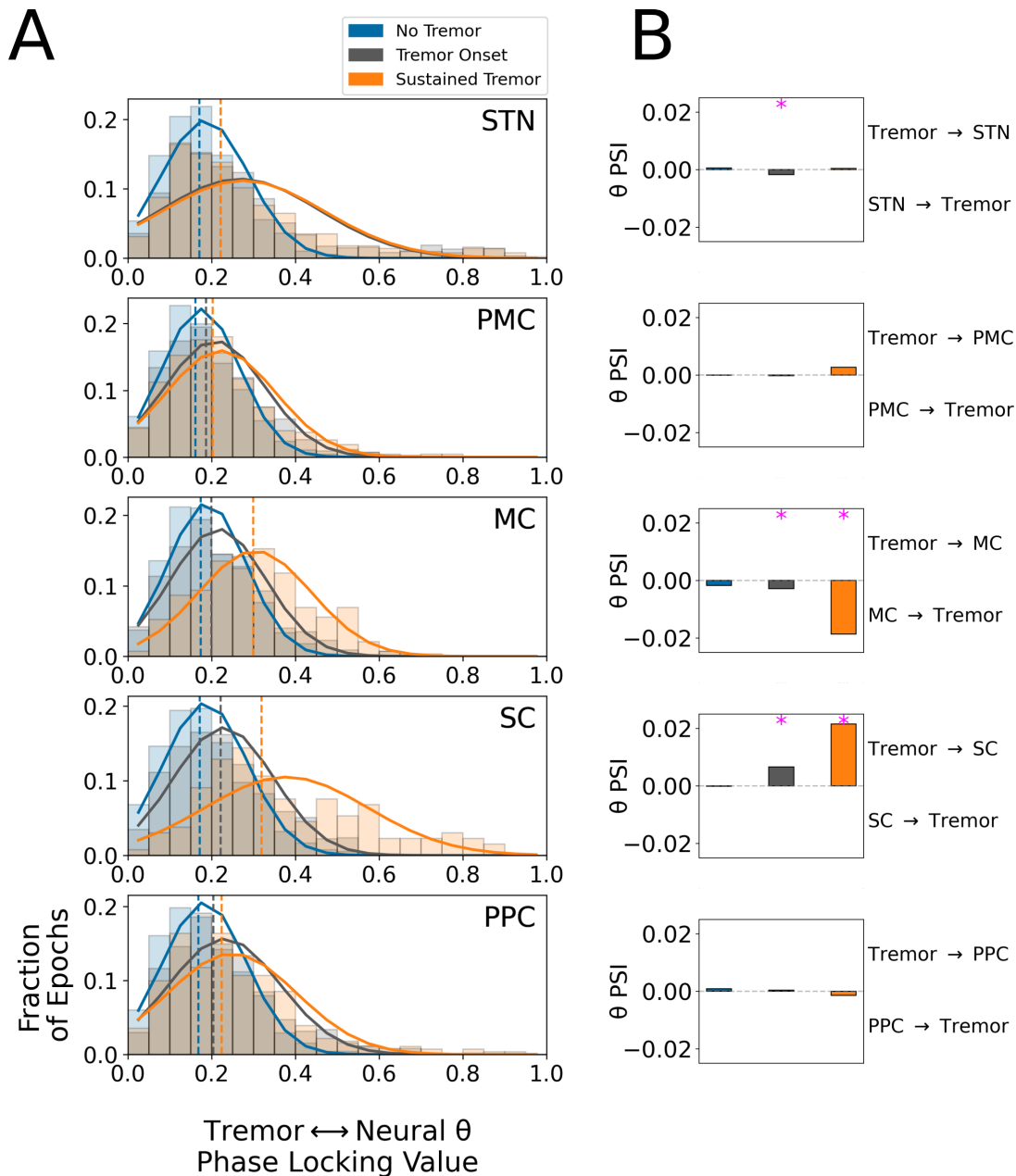


Figure 4. Neural θ exhibited structure-specific temporal relationships with tremor.

A, Histograms of per-trial phase locking values (PLV) between tremor and neural θ by tremor state. Solid lines indicate normal distribution fit to each tremor state PLV histogram, while vertical dashed lines indicate the median of each tremor state PLV histogram. Y-axis indicates proportion of trials within each PLV histogram bin. Note that STN histograms for tremor onset and sustained tremor are highly overlapping.

B, Phase slope index (PSI) between tremor and neural θ by tremor state. Positive values indicated that tremor phase preceded neural phase, while negative values indicated neural phase preceded tremor. Magenta asterisks indicate significant ($p < 0.05$, bootstrap test) PSI effects.

STN - subthalamic nucleus, PMC - premotor cortex; MC - motor cortex; SC - somatosensory cortex; PPC - parietal cortex.

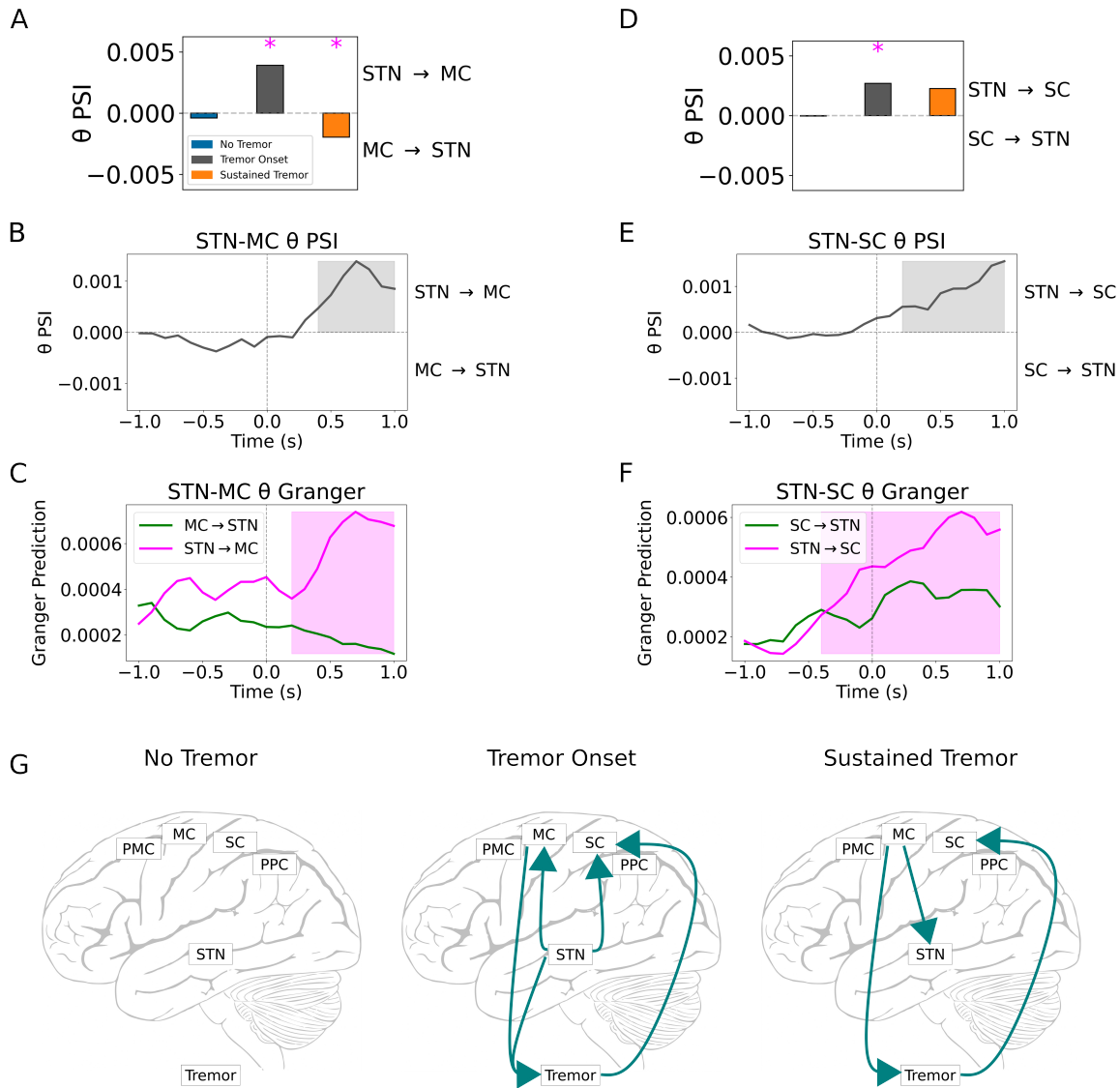


Figure 5. Tremor initiation was driven by the subthalamic nucleus.

A, Static phase slope index (PSI) between STN and MC recordings during tremor states. Magenta asterisks indicate significant ($p < 0.05$, bootstrap test) PSI effects.

B, Dynamic PSI between STN and MC θ during tremor onset. Highlighted regions indicate significant PSI ($p < 0.05$, bootstrap test). Vertical dashed line ($t = 0$) indicates tremor onset trigger.

C, Directed granger prediction (GP) between STN and MC θ during tremor onset. Vertical dashed line ($t = 0$) indicates tremor onset trigger. Highlighted regions indicate significant granger prediction ($p < 0.001$, bootstrap test).

D, Static PSI between STN and SC recordings during tremor states. Magenta asterisks indicate significant ($p < 0.05$, bootstrap test) PSI effects.

E, Dynamic PSI between STN and SC θ during tremor onset. Highlighted regions indicate significant PSI ($p < 0.05$, bootstrap test). Vertical dashed line ($t = 0$) indicates tremor onset trigger.

F, Directed GP between STN and SC θ during tremor onset. Vertical dashed line ($t = 0$) indicates tremor onset trigger. Highlighted regions indicate significant granger prediction ($p < 0.001$, bootstrap test).

G, Summary of θ PSI results. Solid lines represent directed functional connectivity between neural regions and tremor.

STN - subthalamic nucleus; PMC - premotor cortex; MC - motor cortex; SC - somatosensory cortex; PPC - parietal cortex.

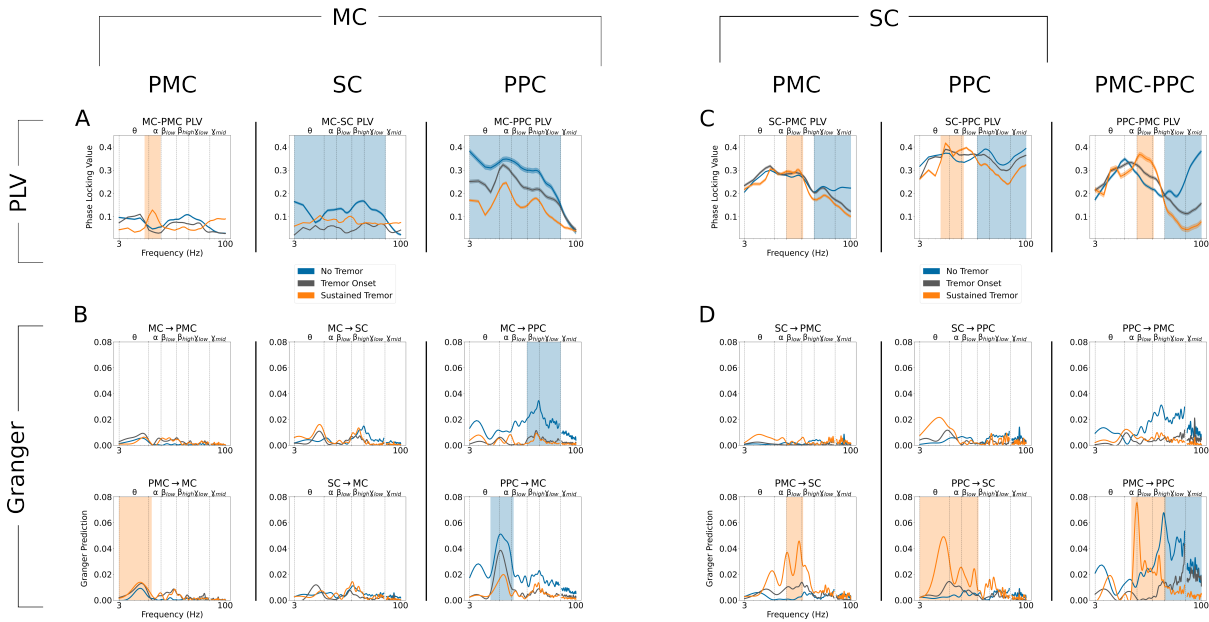


Figure 6. During sustained tremor, gamma coupling between premotor/motor and somatosensory/parietal cortices decreased.

A, Phase locking value (PLV) between MC and other cortical regions. Lines \pm shaded borders represent average \pm standard error PLV. Highlighted frequency ranges indicate increased (orange) or decreased (blue) PLV with increasing tremor.

B, Pairwise granger prediction (GP) between MC and other cortical regions. The title of each subpanel indicates the directionality of the structure pair GP. Highlighted frequency ranges indicate increased (orange) or decreased (blue) GP with increasing tremor. For ease of visualization, curves were lowpass filtered and frequencies within 58–62 Hz were masked. Note that MC broad-spectrum coupling with SC and PPC generally decreased with increasing tremor.

C, PLV between SC and other cortical regions. Lines \pm shaded borders represent average \pm standard error PLV. Highlighted frequency ranges indicate increased (orange) or decreased (blue) PLV with increasing tremor.

D, Pairwise GP between SC and other cortical regions. Title of each subpanel indicates the directionality of the structure pair GP. Highlighted frequency ranges indicate increased (orange) or decreased (blue) GP with increasing tremor. For ease of visualization, curves were lowpass filtered and frequencies within 58–62 Hz were masked. Note that tremor generally shifted the frequency of coupling between SC, PPC, and PMC from γ to α/β_{low} with increasing tremor.

Vertical dashed lines represent frequency band borders. STN - subthalamic nucleus; PMC - premotor cortex; MC - motor cortex; SC - somatosensory cortex; PPC - parietal cortex.

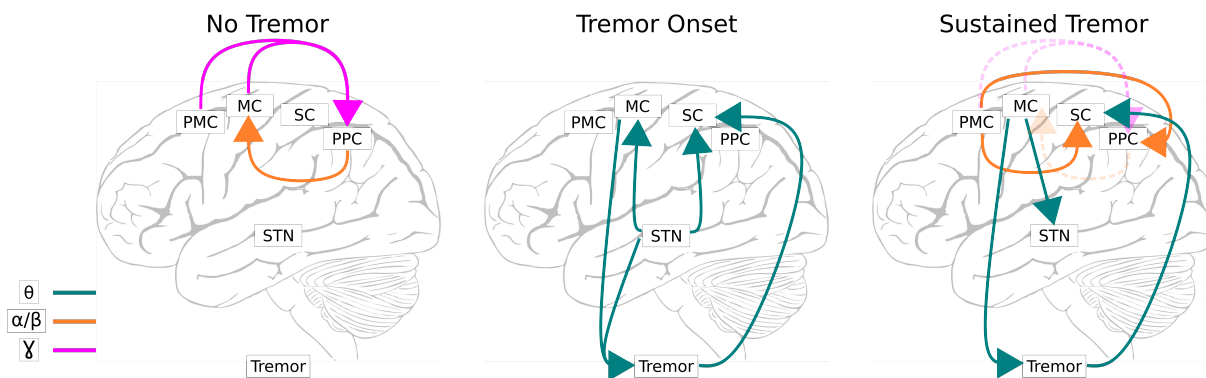


Figure 7. Synthetic model of subcortical-cortical interactions during tremor.

Solid lines represent directed functional connectivity between neural regions and tremor. Dashed lines during sustained tremor represent interactions from the no tremor state that are no longer present.

STN - subthalamic nucleus; PMC - premotor cortex; MC - motor cortex; SC - somatosensory cortex; PPC - parietal cortex.